

THE UNIVERSITY OF CALGARY

A Comparison of a Simple Model of EUV Dayglow with Viking Data

by

Maurice Thomas Shevalier

A THESIS SUBMITTED TO THE FACULTY OF GRADUATE STUDIES IN
PARTIAL FULFILLMENT OF THE REQUIREMENTS FOR THE
DEGREE OF MASTER OF SCIENCE

DEPARTMENT OF PHYSICS AND ASTRONOMY

CALGARY, ALBERTA

FEBRUARY, 1993

© MAURICE THOMAS SHEVALIER 1993



National Library
of Canada

Acquisitions and
Bibliographic Services Branch

395 Wellington Street
Ottawa, Ontario
K1A 0N4

Bibliothèque nationale
du Canada

Direction des acquisitions et
des services bibliographiques

395, rue Wellington
Ottawa (Ontario)
K1A 0N4

Your file *Votre référence*

Our file *Notre référence*

The author has granted an irrevocable non-exclusive licence allowing the National Library of Canada to reproduce, loan, distribute or sell copies of his/her thesis by any means and in any form or format, making this thesis available to interested persons.

L'auteur a accordé une licence irrévocable et non exclusive permettant à la Bibliothèque nationale du Canada de reproduire, prêter, distribuer ou vendre des copies de sa thèse de quelque manière et sous quelque forme que ce soit pour mettre des exemplaires de cette thèse à la disposition des personnes intéressées.

The author retains ownership of the copyright in his/her thesis. Neither the thesis nor substantial extracts from it may be printed or otherwise reproduced without his/her permission.

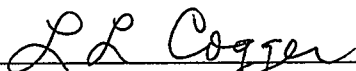
L'auteur conserve la propriété du droit d'auteur qui protège sa thèse. Ni la thèse ni des extraits substantiels de celle-ci ne doivent être imprimés ou autrement reproduits sans son autorisation.

ISBN 0-315-83258-4

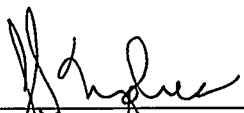
Canada

THE UNIVERSITY OF CALGARY
FACULTY OF GRADUATE STUDIES

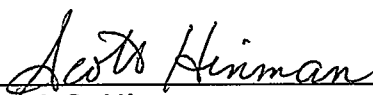
The undersigned certify that they have read, and recommend to the Faculty of Graduate Studies for acceptance, a thesis entitled "A Comparison of a Simple Model of EUV Dayglow with Viking Data" submitted by Maurice Thomas Shevalier in partial fulfillment of the requirements for the degree of Master of Science.



Supervisor, Dr. L.L. Cogger
Department of Physics and
Astronomy



Dr. J.S. Murphree
Department of Physics and
Astronomy



Dr. A.S. Hinman
Department of Chemistry

Feb 12, 1993

Abstract

A simple model of EUV dayglow was developed to determine the origin of double limbs observed by the Viking satellite. A simple model was developed using results from previously published models. The shape and intensities of the calculated profiles match those that appear in the literature.

The Viking altitude/intensity profiles show two peaks present which do not match published or modelled profiles. When the altitude of the upper peak was adjusted to match the modelled peak, the lower peak decreased in altitude from 120 to 9 km, indicating a possible tropospheric source for the lower peak.

The volume emission rate profiles obtained from the model and from altitude corrected inverted Viking data were very similar. The modelled column intensities were significantly larger than the Viking satellite's, so the normalized peak intensities were compared. The peaks have a similar shape with differences attributed to long wavelength leakage in the camera.

Acknowledgements

The author wishes to express gratitude to his supervisor, Dr. Leroy Cogger, for his guidance, encouragement and patience throughout this program.

The author is grateful to the patience of Ian Hutcheon who always encouraged me to continue.

Thanks also go to Brian Fong and Andrew Macrae who always listened to my complaints and gripes.

A special thanks to Cliff Marcellus who was always there to answer my dumb computing questions and problems and for those many "Liquid State Seminars" which helped me throughout the years.

to Shelley, Alex and Jonathan:

for love, patience, understanding and encouragement

Table of Contents

	Page
Approval Page	ii
Abstract	iii
Acknowledgements	iv
Dedications	v
Table of Contents	vi
List of Tables	ix
List of Figures	x
List of Symbols	xiv
Chapter 1 Introduction	1
1.1 Dayglow	3
1.2 The Viking Satellite	4
1.3 Emission Bands	6
1.3.1 Lyman-Birge-Hopfield Bands	6
1.3.2 Atomic Oxygen Emission, O I 135.6 nm	7
1.3.3 Atomic Nitrogen Emissions, N I	8
1.4 Purpose of this Study	9
Chapter 2 A Literature Survey of Molecular Nitrogen	11
Chapter 3 Viking Images	15
3.1 Inversion of Slant Column Intensities	15
3.2 Investigation of the Viking Data Base	17
3.3 Orbits 1386 and 1485	17
3.4 Calculation of Dayglow Tangent Altitudes	20
3.5 Slant Column Intensity/Volume Emission Rate Profiles	23
Chapter 4 Model Development	25

	Page
4.1 Neutral Density, $\rho(z)$	25
4.2 Cross Sections, $\sigma(E)$	28
4.3 Photoelectron Flux, $F(z,E)$	31
4.3.1 EUV Flux	33
4.3.2 Electron and Neutral Temperature	35
4.3.3 Electron Density	36
4.3.4 Photoelectron Flux	40
4.4 Schumann-Runge Bands	41
4.5 Volume Emission Rates	42
4.6 Slant Column Intensity	43
4.7 Column Intensity	47
Chapter 5 Discussion	49
5.1 Modelled Results	49
5.1.1 Neutral Concentration and Temperature Profiles	49
5.1.2 Photoelectron Flux	51
5.1.3 Volume Emission Rate	52
5.1.4 Column Intensity	53
5.2 Comparison of Modelled Results to Published Data	55
5.2.1 Photoelectron Flux	55
5.2.2 Column Intensity	58
5.3 Viking Data Results	61
5.3.1 Comparison of the Volume Emission Rate Profiles	61
5.3.2 Comparison of Column Intensity Profiles	64
Chapter 6 Conclusions and Future Work	69
6.1 Conclusions	69

	Page
6.2 Future Work	72
References	73
Appendix 1 Viking Orbits Which Contain Double Limbs	80
Appendix 2 Computer Model Outline	92

List of Tables

	Page
Table 1-1 Reactions Which May Cause Airglow	4
Table 4-1 Input Data for the MSIS-86 Program for the Viking Orbits	27
Table 4-2 LBH Emission Bands of Interest and Their Branching Ratio	30
Table 4-3 EUV Ratios for Viking Orbits of Study	35
Table 4-4 Ion Chemical Reactions and Rate Coefficients	39
Table 4-5 LBH Branching Ratios at Different Altitudes Due to Schumann-Runge Absorption	42
Table 4-6 Satellite Parameters used in Calculating Column Intensity	47
Table 5-1 Parameters Used in Model Calculations for Solar Minimum and Maximum Conditions	50
Table 5-2 Geophysical Parameters Relevant to the 1978 Photoelectron Flux Calculations	57
Table 5-3 Geophysical Parameters for the 1980 Rocket Flight	59

List of Figures

	Page
Figure 1.1 Concentrations of molecules and atoms as a function of altitude for the earth's atmosphere.	1
Figure 1.2 The concentration of some ions as a function of altitude for the earth's atmosphere	2
Figure 1.3 Temperature as a function of altitude	2
Figure 1.4 A partial potential energy diagram for N ₂ showing the Lyman-Birge-Hopfield emission bands	7
Figure 1.5 Partial energy level diagram for O I	8
Figure 1.6 Partial energy level diagram for N I	9
Figure 3.1 Limb scanning geometry of a satellite	16
Figure 3.2 Viking satellite image for a) Orbit 1386 b) Orbit 1385	18
Figure 3.3 Raw altitude/intensity profiles for orbits: a) 1386 99.019 b) 1485 99.032	19
Figure 3.4 Geometry used to determine the altitude of the double limbs	22
Figure 3.5 Tangent altitude/slant column intensity profiles for a) 1386 99.019 b) 1485 99.032 calculated based upon the simple geometry given in Figure 3.4	22
Figure 3.6 Tangent altitude/slant column intensity profiles for a) 1386 99.019 b) 1485 99.032.	24
Figure 3.7 Altitude/Volume Emission Rate profiles for a) 1386 99.019 b) 1485 99.032	25

	Page
Figure 4.1 Concentrations of N, O, O ₂ and N ₂ as a function of altitude calculated by the MSIS-86 program for a) 1386 99.019 b) 1485 99.032	28
Figure 4.2 Cross sectional areas as a function of energy	31
Figure 4.3 The H L- α measurements from 1969 to 1988, showing the satellites that collected the data and the Solar Cycles.	34
Figure 4.4 The electron and neutral temperatures versus altitude for orbits a) 1386 99.019 b) 1485 99.032	37
Figure 4.5 Altitude/Electron concentration profiles for orbits 1386 99.019 and orbits 1485 99.032	38
Figure 4.6 The calculated photoelectron flux as a function of energy for Viking orbits a) 1386 99.019 b) 1485 99.032	40
Figure 4.7 Schumann-Runge O ₂ absorption cross section and altitude of O ₂ absorption of LBH lines	41
Figure 4.8 Volume emission rate at various altitudes for orbits a) 1386 99.019 b) 1485 99.032	44
Figure 4.9 Tangent altitude/slant column intensity profiles for a) 1386 99.019 b) 1485 99.032	46
Figure 4.10 Modelled altitude/column intensity profiles as seen by a rocket for a) Orbit 1386 b) Orbit 1485	48
Figure 5.1 Atmospheric concentrations from the MSIS-86 model for solar minimum and solar maximum	50

	Page
Figure 5.2 Neutral atmospheric temperatures from the MSIS-86 model at solar minimum and maximum	51
Figure 5.3 Photoelectron flux versus energy for solar minimum and solar maximum at a) 150 km b) 250 km	52
Figure 5.4 Volume emission rates at different altitudes at solar minimum and solar maximum for a) LBH bands b) OI 1356	53
Figure 5.5 Tangent altitude/slant column intensity profiles for a) Lyman-Birge-Hopfield Bands b) OI 1356 as viewed by a satellite	54
Figure 5.6 Altitude/Intensity profiles for a) Lyman-Birge-Hopfield b) OI 1356 as viewed by a rocket	54
Figure 5.7 Comparison between different photoelectron flux models for an altitude of 170 km	57
Figure 5.8 A comparison of results from this model, the model of Link et al. (1988) and 1980 rocket results for a) OI at 135.6 nm b) LBH band at 144.5 nm	59
Figure 5.9 Adjusted altitude/VER profiles for orbits 1386 99.019 and 1485 99.032	62
Figure 5.10 A comparison of altitude/VER profiles obtained from the Viking satellite and the model for orbits a) 1386 99.019 b) 1485 99.032	63
Figure 5.11 Camera 0 sensitivity as a function of wavelength	65

	Page
Figure 5.12 Modelled altitude/DN profiles for orbits 1386 and 1485.	65
Figure 5.13 Altitude corrected altitude/intensity profiles for Orbits 1386 and 1485	66
Figure 5.14 Altitude/DN ratio for orbits 1386 and 1485	67
Figure 5.15 A comparison of altitude/normalized DN for the calculated profile, corrected and uncorrected observed profiles for a) Orbit 1386 b) Orbit 1485	67

List of Symbols

$[X]$	concentration of species X
CI	column intensity
$F(z,E)$	photoelectron flux at an altitude z and energy E
h	perpendicular height
$I_i(h)$	observed intensity at height h
$J(z),j(z)$	volume emission rate at an altitude z
J_i	production frequency of species i
$L(z,h)$	optical path length at height h for layer at altitude z
LBH	Lyman-Birge Hopfield
L_{eE}	loss due to thermal electrons
N I	atomic nitrogen
O I	atomic oxygen
S_{EUV}	solar cycle attenuation due to EUV flux
T	neutral temperature
T_e	electron temperature
VER	volume emission rate
z	altitude
α	angle formed from center of earth to satellite to surface of earth
λ	wavelength
θ	angle formed from surface of earth to satellite to layer of atmosphere under study.
$\rho(z)$	neutral density
$\sigma(E)$	cross section at energy E
τ	optical thickness of atmosphere

CHAPTER 1 INTRODUCTION

The earth's atmosphere above 100 km is a very complex system which is composed of many different molecules and atoms in varying amounts. The concentration of these molecules and atoms changes as a function of altitude. For neutral molecules, the concentration tends to decrease as the altitude increases as shown in Figure 1.1. For ions, such as NO^+ and O_2^+ , the concentration has two peaks, one at 105 km and the second at 170 km. For N_2^+ and O^+ the peak increases then decreases as the altitude increases (Figure 1.2).

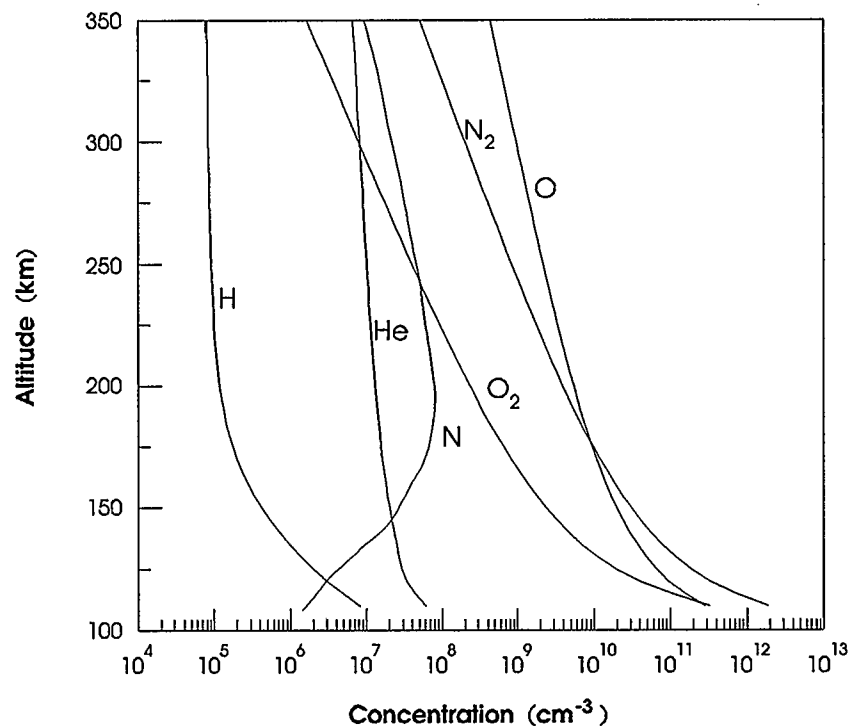


Figure 1.1 Concentrations of molecules and atoms as a function of altitude for the earth's atmosphere. (From MSIS-86 calculation)

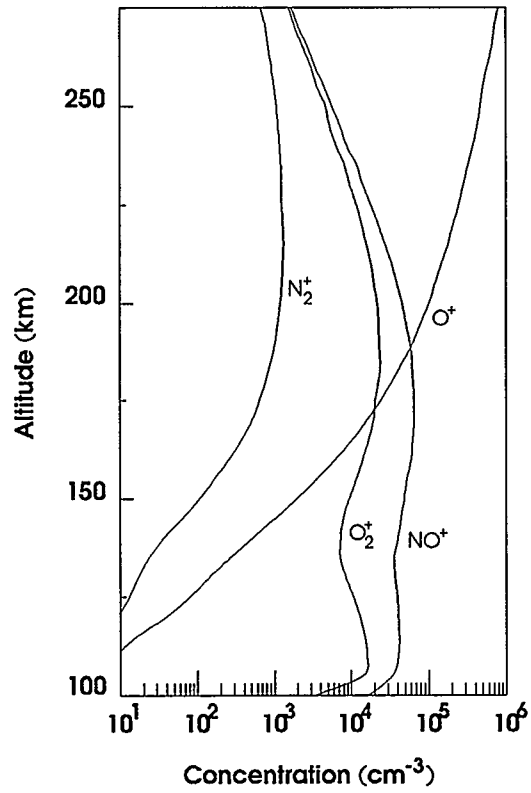


Figure 1.2 The concentration of some ions as a function of altitude for the earth's atmosphere

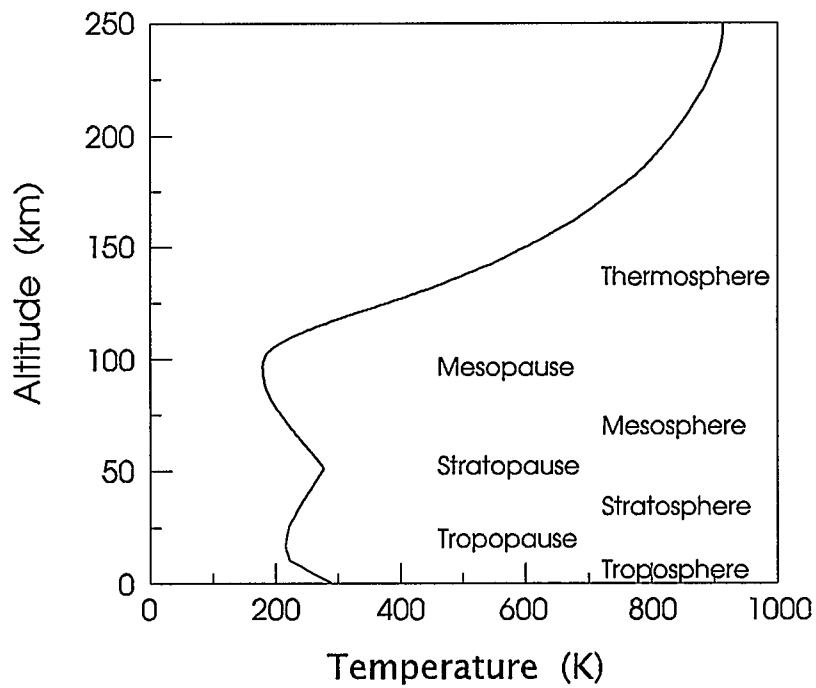


Figure 1.3 Temperature as a function of altitude.

The temperature of the atmosphere also changes as altitude increase but not monotonically.. It decreases with altitude in the troposphere and the mesosphere and increases in the stratosphere and the thermosphere (see Figure 1.3) (Banks and Kockarts 1973).

1.1 Dayglow

The atoms and molecules in the earth's atmosphere absorb energy and as a result they emit radiation both during the day and night, producing aurora and airglow. Airglow is "the amorphous, optical radiation continuously emitted by ...(the) atmosphere ... from the far ultraviolet into the near infrared ..." (Chamberlain and Hunten, 1987). Aurora is "an optical emission from the upper atmosphere ...(whose) source of excitation (is) impact of electrons and ions precipitated from outside the atmosphere" (Chamberlain and Hunten, 1987). Airglow can be distinguished from aurora on the basis of the aurora's geographic confinement to magnetic polar and subpolar regions and due to its sporadic occurrence.

Airglow arises from the discrete atomic and molecular emissions resulting in an emission line and emission band spectrum in the atmosphere. The daytime emissions, or dayglow, come from the chemical reactions occurring in the ionosphere and from the scattering of sunlight as well as radiation emitted from photochemical reactions generated by energetic photoelectrons (Chamberlain and Hunten, 1987). Airglow emission lines or bands which are present in the

atmosphere originate from one or more of the reactions listed in Table 1.1 (Rees, 1989). Other sources of dayglow are resonant scattering and fluorescence.

Table 1.1 Reactions which may cause Airglow

Chemical Reaction	Reaction Type
$h\nu + A \rightarrow A^* + k.e.$	Photon impact excitation
$h\nu + A \rightarrow A^{**} + e^-$	Photon impact ionization excitation
$h\nu + AB \rightarrow A^* + B^* + k.e.$	Photodissociative excitation
$e^- + A \rightarrow A^* + e^-$	Photoelectron excitation
$e^- + A \rightarrow A^{**} + 2e^-$	Photoelectron ionization excitation
$e^- + AB \rightarrow A^* + B + e^-$	Photoelectron impact dissociative excitation
$e^- + AB \rightarrow A^{**} + B^* + e^-$	Photoelectron dissociative ionization excitation
$e^- + A^+ \rightarrow A^* + h\nu$	Dielectronic Recombination
$e^- + A^+ \rightarrow A + h\nu$	Radiative Recombination
$e^- + AB^+ \rightarrow A^* + B$	Dissociative Recombination

A signifies either an atom or a molecule, AB signifies a molecule and the asterisk indicates the formation of an excited state.

1.2 The Viking Satellite

The observation of emissions from the atmosphere has long been of interest since an understanding of these processes would help to improve our comprehension of the atmosphere. The observations of the

emissions, however, has been difficult since in many cases they are not observable from the surface of the earth. Rockets and balloons have been, and still are, used to observe the emissions, but the observation time is very short. More recently, satellites have been used to observe these emissions. The satellites stay in orbit for a much longer time and have allowed a very large data base to be accumulated. This has led to a greater understanding of the processes that occur in the atmosphere.

Viking was such a satellite, launched by the Swedish Space Corporation. This satellite was specifically designed for "the study of physical processes in the medium altitude range on auroral field lines" (Hultqvist 1987). The Viking satellite had a total of five instruments which were designed to investigate different regions of the auroral processes. One instrument consisted of two cameras, one designed to cover the 123.5 to 160.0 nm range (camera 1) and the other to cover the 134.0 to 180.0 nm range (camera 0). Camera 1 was designed to observe the strong 130.4 nm and the 135.6 nm O I lines as well as some of the N₂ Lyman-Birge-Hopfield (LBH) bands. Camera 0 was designed to cut off the O I lines but to pass the LBH bands (Anger et al., 1987).

This satellite was not specifically designed to monitor dayglow. However, as the satellite moved in its orbit, images of the atmosphere above the earth's surface are seen. On these satellite images bright regions, which appear as thin bands, become visible. These bands, also known as limbs, are regions where chemical reactions in the earth's atmosphere are emitting light which is visible to the satellite's cameras. From these limbs, the dayglow process can be studied.

1.3 Emission Bands

In the wavelength range from 134 to 180 nm, the wavelength range of camera 0 of the Viking satellite, many emission bands are observed. The predominant emissions in this wavelength region are bands from the Lyman-Birge-Hopfield emission of N_2 , the line emission of O I at 135.6 nm and the N I emissions at 149.3 and 174.4 nm.

1.3.1 Lyman-Birge-Hopfield Bands

The Lyman-Birge-Hopfield (LBH) bands are caused by the collision of a photoelectron and a N_2 molecule resulting in an excited N_2 molecule. This excited N_2 molecule then de-excites to a ground state with the emission of a photon. More specifically, the LBH emissions are due to transitions from the $a^1\Pi_g$ band to the $X^1\Sigma_g^+$ band (see Figure 1.4), which are electric dipole forbidden. The large number of emission bands are due to the large number of states available. In the region from 125 to 180 nm, 60 bands have been observed due to different LBH transitions (Ajello and Shemansky, 1985).

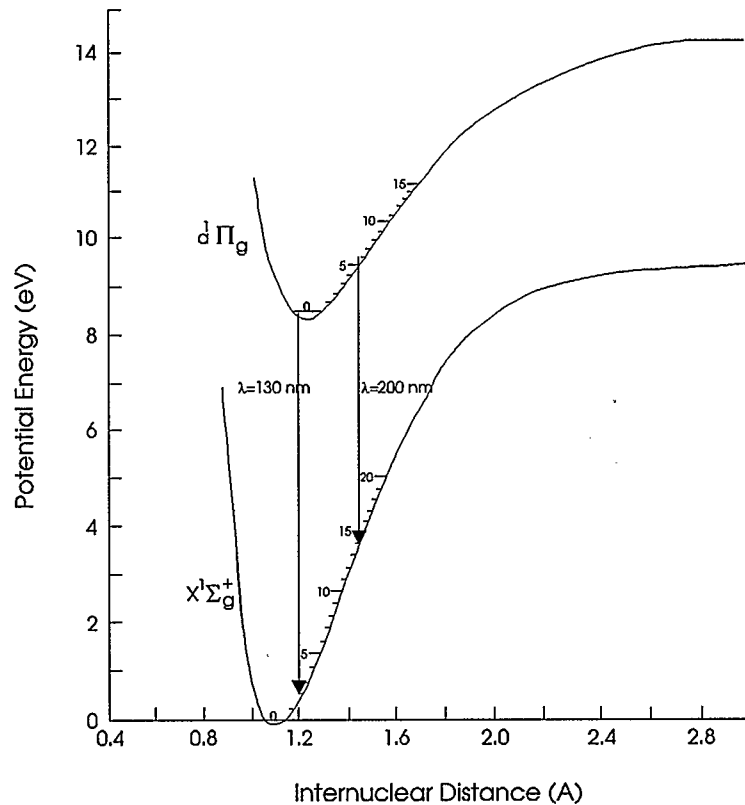


Figure 1.4 A partial potential energy diagram for N_2 showing the Lyman-Birge-Hopfield emission bands. Adapted from Meyerott and Swenson (1990).

1.3.2 Atomic Oxygen Emission, O I 135.6 nm

Figure 1.5 shows the different emission lines that have been observed in airglow and aurora from atomic oxygen, O I. In the wavelength range of interest on the Viking satellite, only one emission, the O I 1356 emission, is visible at 135.6 nm. This is caused by the spin forbidden transition from the $3s\ ^5S$ to the $2p^4\ ^3P$ band and is a predominant feature in dayglow. This emission is, in fact, the sum of two lines in a

doublet, ${}^3P_2 - {}^5S_2$ and ${}^3P_1 - {}^5S_2$, with wavelengths of 135.55977 nm and 135.85123 nm respectively (Meier, 1991).

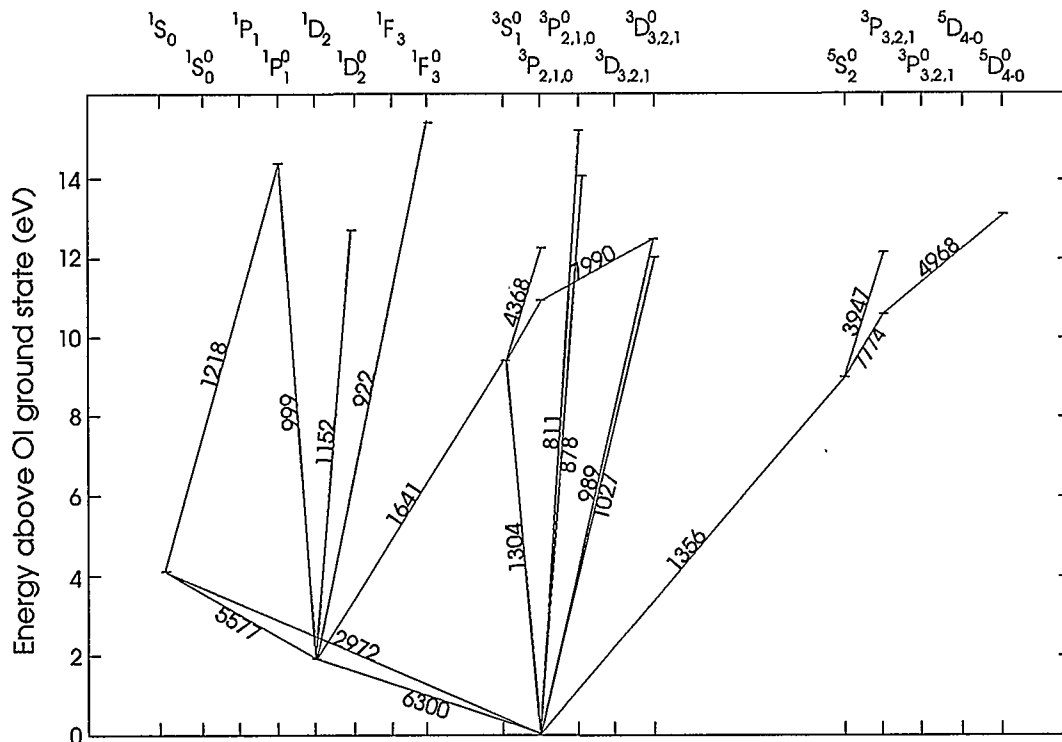


Figure 1.5 Partial energy level diagram for O I. Adapted from Rees (1989).

1.3.3 Atomic Nitrogen Emissions, N I

In the wavelength range of the Viking camera, two main atomic nitrogen, N I, emission lines are present at 149.3 nm and 174.4 nm. Of the two the 149.3 nm line is the brighter. Figure 1.6 shows a partial energy level diagram for atomic nitrogen showing some of the transitions that have been observed in the airglow or aurora (Rees, 1989).

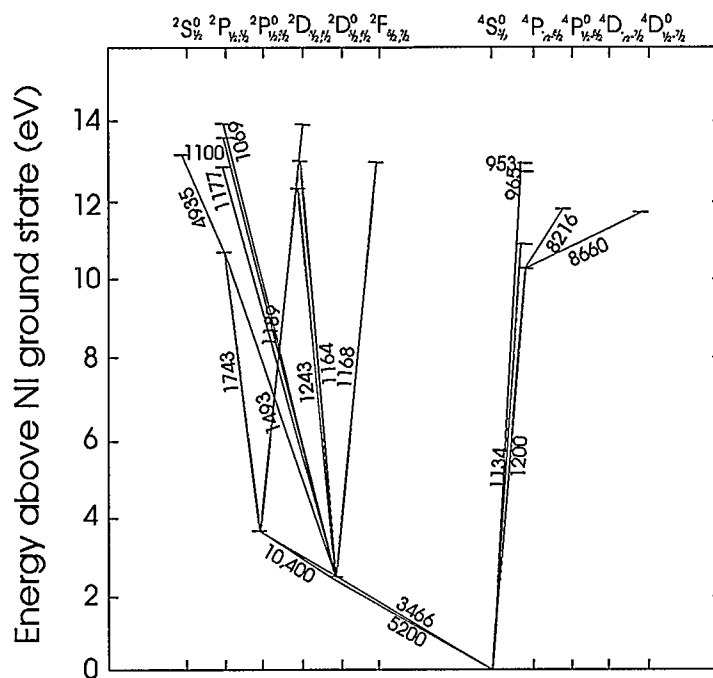


Figure 1.6 Partial energy level diagram for Ni I. Adapted from Rees (1989).

1.4 Purpose of this Study

In this study, altitude/intensity profiles obtained from the Viking satellite data base are compared to results from a simple model which has been developed for this study. The input to the model includes the location of the study area, time of day and a number of geomagnetic indices. The results of the simple model are compared with the Viking satellite data and with other published results. The simple model was developed to allow quick, diagnostic modelling of the EUV dayglow profiles as viewed by either satellites or rockets.

The thesis has been organized in the following manner:

Chapter two surveys the literature that has been published on the LBH emissions.

Chapter three shows the data obtained from the Viking satellite data base that is used in this study.

Chapter four goes over the development of the model.

Chapter five examines the results obtained from the model and compares it to the data obtained from the Viking satellite data base and to other published results.

Chapter six lists the conclusions of the study and recommendations for future work.

CHAPTER 2 A Literature Survey of Molecular Nitrogen

The Viking satellite was designed to monitor the far ultra-violet spectrum of the atmosphere in the wavelength range of 134 to 180 nm, the region of the LBH Bands. Unfortunately even though N_2 is the most abundant molecule in the lower atmosphere, there has not been a great deal of literature in the last decade dealing with the LBH bands.

Kopp et al. (1977) examined the volume emission rate for the second positive (2PG) system of N_2 as observed by the Atmosphere Explorer-C satellite. These data were compared to calculated emission curves. In their calculations, the photoelectron flux of Victor et al. (1976) was used as well as measured neutral densities. They found that the calculated volume emission rates were 20-25% lower than the observed rates.

Meier et al. (1980) considered the far UV emissions from N I and some LBH bands from a rocket flight and compared these observations to calculated volume emission rates. In their calculations, the neutral densities were obtained from the atmospheric model of Jacchia (1971). The photoelectron fluxes used were those of Oran and Strickland (1978). In all cases they found that there was agreement between the theoretical calculations and the observed emission rates.

Conway (1982) calculated the column emission rate of different LBH bands. This was done using resonant scattering theory and a line by

line synthesis of individual bands. The calculated emissions and observed rocket emissions have similar shapes. To get good agreement between the observed and the calculated emissions the photoelectron energy flux needed to be multiplied by 0.7.

Hernandez et al. (1983) compared the predicted and measured volume emission rates from the 2PG band of N_2 from the Atmosphere Explorer C (AE-C) satellite at various altitudes to calculated volume emission rates. Also measured were photoelectron spectra at various altitudes. With the measured N_2 density and the theoretical photoelectron flux, a calculated volume emission rate was obtained and compared to the measured volume emission rate. They found that the N_2 2PG emission bands were underestimated by 30% when the theoretical photoelectron fluxes were used. Further when the measured photoelectron fluxes from the AE-C were used, the calculated intensity of the N_2 2PG emissions was highly variable. The cause of this variability was rationalized as spacecraft shielding of the photoelectron spectrometer.

In 1983, Meier and Anderson published a paper on using different LBH bands as well as the 135.6 nm O I line to determine temperature and composition of the atmosphere. Here, several LBH bands were measured using the Atmosphere Explorer satellites and these were compared to modelled emissions. In their models, Meier and Anderson used the Jacchia model atmosphere (1971 or 1977) as well as the photoelectron model of Strickland and Meier (1982). They found that the modelled volume emission rates are sensitive to atmospheric composition. For example, the peak production rate of the N_2 2PG band

at 337.1 nm increases in altitude as the N₂ concentration is increased. This change is due to the solar ionizing flux being deposited at a higher altitude. As the O concentration is increased the volume emission rate is decreased due to a competition for the photoelectron flux energy.

The N₂ 2PG band was observed by Conway and Christensen (1985). Here a rocket carried a photometer and observed the N₂ and O dayglow during solar maximum. They modelled the 337.1 nm results using the photoelectron code of Strickland and Meier (1982) as well as both the Jacchia model atmosphere (1977) and the MSIS-83 model atmosphere (Hedin, 1983). They found, from the modelling results, that the observed volume emission rates at 337.1 nm were due not only to the 2PG N₂ band but also due to the Vegard-Kaplan band of nitrogen, a $A^3\Sigma_u^+ - X^1\Sigma_g^+, (0,9)$ transition.

In 1988 Link et al. re-examined the data from some rocket measurements of the UV dayglow. In the recalculations of the intensity of the emission, the MSIS-83 model (Hedin, 1983) atmosphere was used along with the two stream photoelectron model with a radiative transfer model (Link et al., 1988). Several different LBH bands were used and they found a better agreement between the two sets of data.

Morrison et al. (1990) examined the EUV dayglow at high spectral resolution from a rocket flight. In the modelling of the data, the MSIS-83 (Hedin, 1983) model atmosphere was used along with the two stream photoelectron flux model of Strickland and Meier (1982). They found

that the observational data and the theoretical data agreed when the calculated volume emission rates were scaled up by a factor of 1.4.

It is evident from the literature that the studies conducted to date deal with the examination of monochromatic lines. The Viking cameras are broad band detectors, i.e. they measured the intensity over a wavelength range. This will make a comparison between the model and modelled results which appear in the literature more difficult. Further, it appears that this study is unique since it examines day glow from a broad band viewpoint, and not using monochromatic lines as do other researchers.

Chapter 3 Viking Images

When a satellite measures the intensity of an emission from the earth's limb, it measures the tangent altitude/slant column intensity, i.e. the intensity which is the sum of all emissions from all the layers along a given line of sight. Thus, the intensity can change with different lines of sight. To better understand the data that the satellites and rockets return and ultimately the processes causing dayglow, the emissions at each altitude in the atmosphere must be examined.

3.1 Inversion of Slant Column Intensities

Consider the atmosphere above the earth to be composed of several layers, much as an onion is (see Figure 3.1). The perpendicular height from the surface of the earth to a given layer is h . The distance between two of these layers of atmosphere is z . The relationship between the observed column intensities, CI , at an altitude h , $I_i(h)$, and the corresponding unknown volume emission rate, $J(z)$ are defined by equation (3.1) (Meier, 1991):

$$I_i(h) = \int_0^{\infty} J(z)dL(z,h) \quad (3.1)$$

In the above equation, L is the optical path length. This is the distance between adjacent layers of atmosphere at altitude h to be observed by camera pixel i . In Figure 3.1 the total intensity at pixel i is the sum of all of the emissions from the various layers along the camera's line of

sight. L_{ij} is the total distance traveled by the photon between two layers of atmosphere of shell j . From Figure 3.1 L_{ij} is the distance that the photons from layer i must travel. There are two parts to this emission, the emission due to that part of the layer which is on the satellite side of the observation location and the emission which is located on the other side of the observation location. Equation 3.1 can also be represented as a matrix equation:

$$I = L J \quad (3.2)$$

Thus, the solution to the above matrix equation is:

$$J = L^{-1} I \quad (3.3)$$

The inversion program, so named because of the above operation, written by Rochon (1985) solves the above equation.

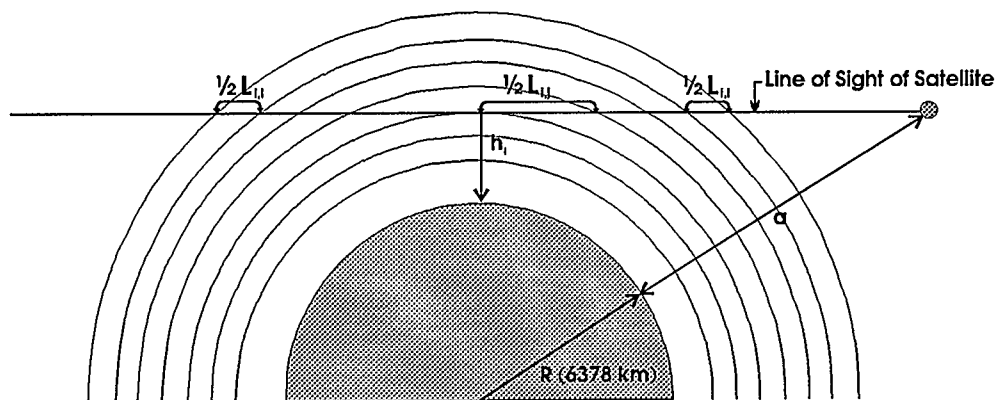


Figure 3.1. Limb scanning geometry of a satellite.

Adapted from Rochon (1985).

3.2 Investigation of the Viking Data Base

The Viking satellite was designed to be a top-down satellite, i.e. it was designed to view the top of the earth's atmosphere. Fortunately, during its orbit, pictures of the atmospheric limb were taken as the satellite approached the perigee of its orbit. These images needed to be identified in the Viking data base. An intensive search of the Viking data base, in which each orbital frame was viewed individually, yielded 102 orbital frames which were thought to contain both limb views of the earth as well as dayglow. Appendix 1 contains a summary of the data of the 102 orbital frames.

3.3 Orbits 1386 and 1485

This study will concentrate on two specific orbital frames from the Viking data base, orbit 1485, frame reference number 99.032 and orbit 1386, frame reference number 99.019. These frames were chosen because they had a minimum of auroral contamination and the contamination was not near the center of the frame. These two orbital frames are shown in Figure 3.2. From this figure, it is apparent that there are definite double limbs visible. Below both limbs are aurora, but these are not contaminating the double limb images. The bottom one third of the image is the image from the camera's baffle, which is closing to protect the camera from the sunlight.

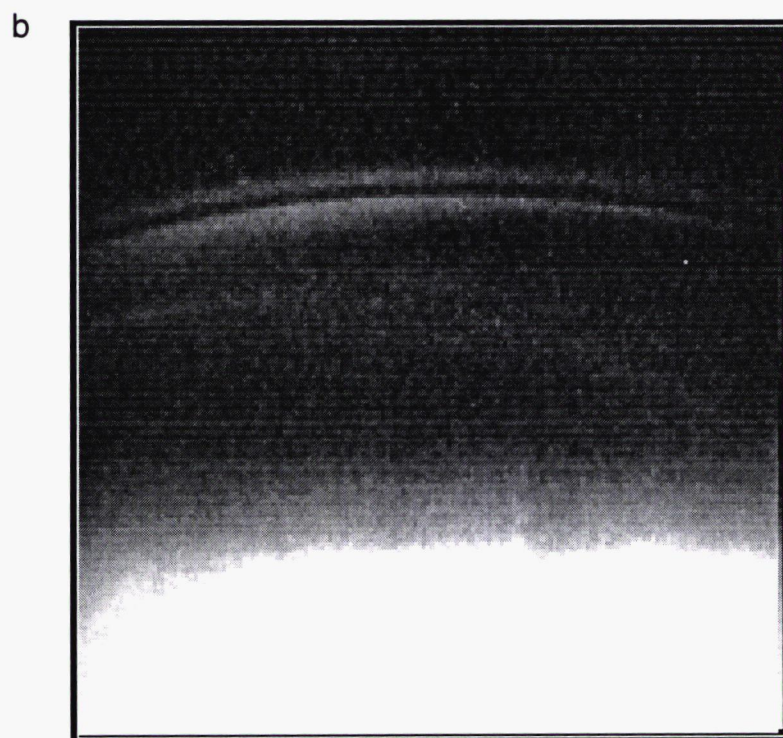
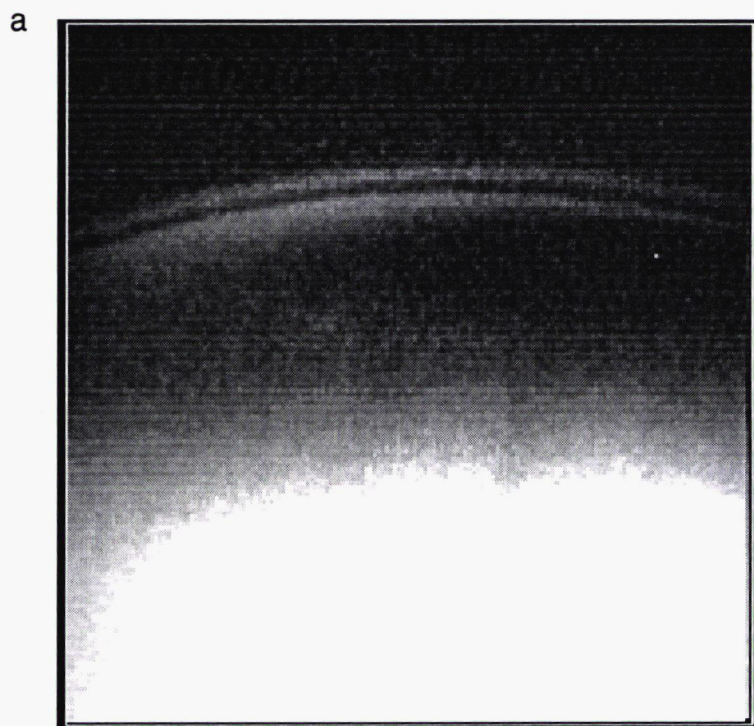


Figure 3.2 Viking satellite image for
a) 1386 99.032 b) 1485 99.032

The average of columns 231 to 237 are shown in Figure 3.3. The intensity given in these plots are in data numbers, DN, since the data base contains only intensity values from 0 to 255. From these figures, it can be seen that there are definitely two peaks present. These peaks occur near vertical pixel numbers 85 and 100. According to the Viking data base these columns are at a longitude of 178.4° east and 164.78° east for orbits 1485 and 1386 respectively. Given this and the universal time for the orbits, the calculated local solar times of the two points are 10.4 and 12.29 hours (based on a 24 hour clock) for 1386 and 1485 respectively, definitely daylight hours. Thus these peaks are probably due to dayglow.

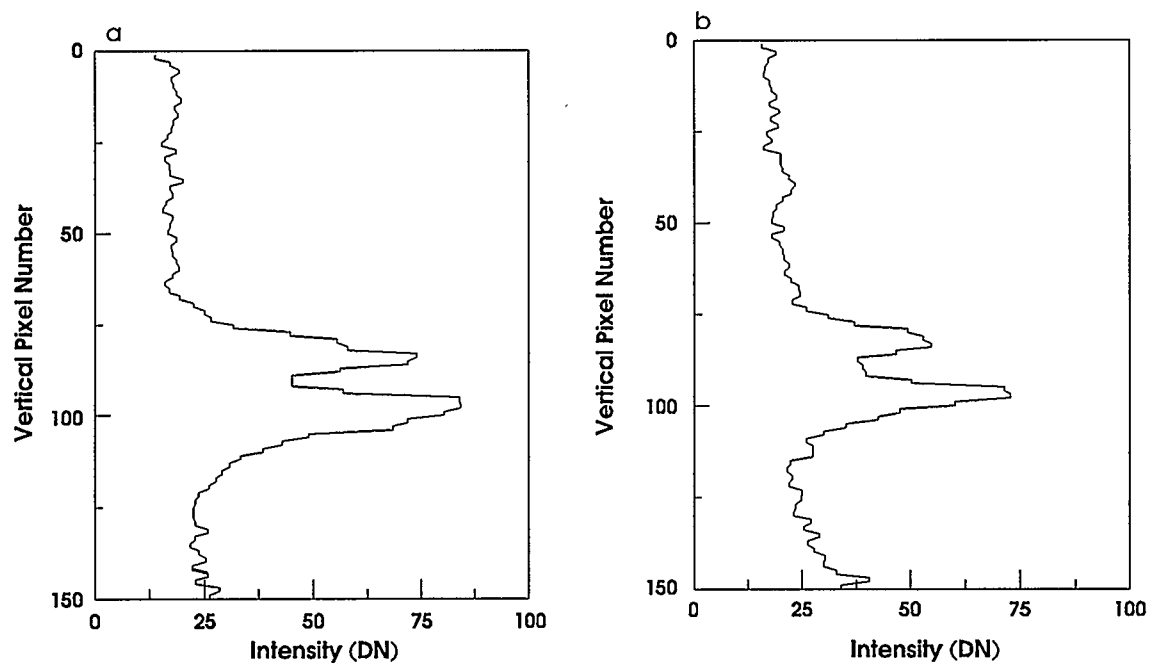


Figure 3.3 Raw altitude/intensity profiles for orbits:

a) 1386 99.019 b) 1485 99.032

3.4 Calculation of Dayglow Tangent Altitudes

The exact altitudes in the tangent altitude/slant column intensity (altitude/intensity) profile is not provided by the satellite database since the satellite was designed as a topside satellite, i.e. it is designed to view the surface of the atmosphere and not limbs. The altitude can be calculated indirectly from stars which are viewed in the frame. By adjusting the right ascension and declination of the spin axis of the satellite, the calculated right ascension and declination of a star changes. When the star's calculated right ascension and declination merge with the star's image the altitude of the bands on the image can be calculated. All of these calculations are done using xsystem, the software associated with the Viking database. This was done with two different orbits which had a star visible, orbits 1485 99.033 and orbits 1396 99.021. Here the lower limb altitude in both cases corresponded to 120 km. While this technique is not exact, it does give a first approximation to the altitude of the lower limb, to which the slant altitude/intensity profiles were referenced.

The tangential altitudes which correspond to columns 231 to 235 were then calculated. This was done from simple geometry and assuming that the lower peak has an altitude of 120 km. Figure 3.4 shows the geometry for the double limbs. The dotted line represents the lower limb, which was set at an altitude of 120 km and the upper thick line represents the upper limb. 'R' in the figure represents the radius of the

earth and 'a' represents the altitude of the satellite from the center of the earth. α is the angle from the surface of the earth to the satellite to the center of the earth and is a constant angle. Now consider the satellite 'looking' at the lower limb. The new angle formed from the satellite's orbital position to the lower limb is $\alpha + \theta$. Since the altitude of the lower limb is known, and the radius of the earth is known, the angle θ can be calculated from simple geometry,

$$\sin \alpha = R/a \quad (3.4)$$

$$\sin(\alpha+\theta) = (h+R)/a \quad (3.5)$$

Finally, knowing that the angular resolution, k , of the camera is 0.0768 degrees, if the line of sight is moved up by one pixel, a new angle θ' can be calculated, given that $\theta' = \theta + nk$, and thus a new altitude h for that pixel is given by:

$$h = a(\sin(\alpha + \theta')) - R \quad (3.6)$$

In this manner, the tangential altitudes of the altitude/intensity profiles were calculated. The new altitude/intensity profiles are shown in Figure 3.4. From this figure it can be seen that the lower limb has a higher intensity in both cases. The second peak is broader than the first limb. The maximum intensities in 1485 occur at 120 and 240 km and for 1386 they occur at 120 and 280 km.

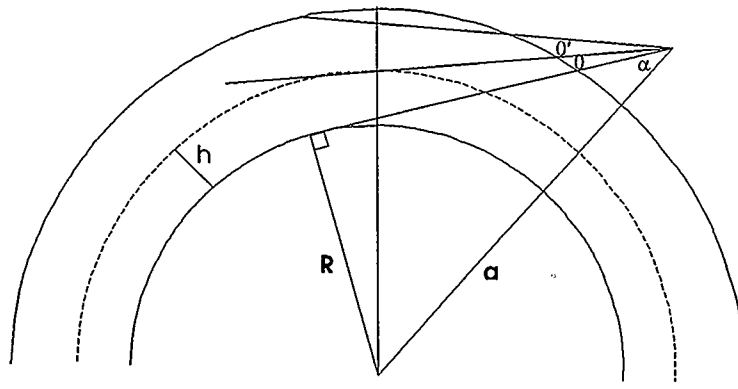


Figure 3.4 Geometry used to determine the altitude of the double limbs. See the text for details.

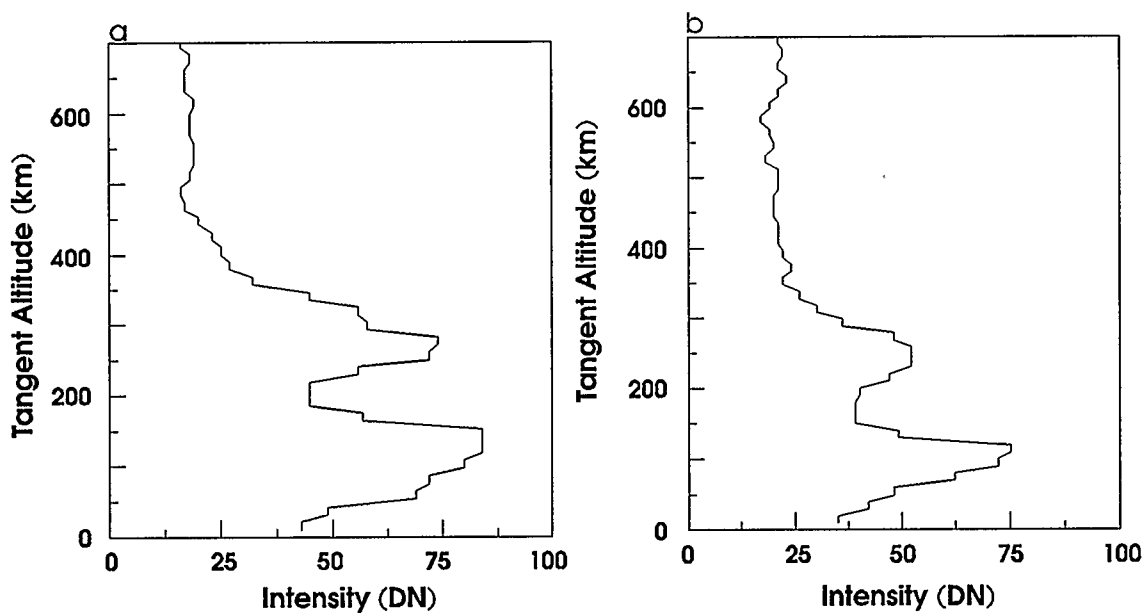


Figure 3.5 Tangent altitude/slant column intensity profiles for a) 1386 99.019 b) 1485 99.032 calculated based upon the simple geometry given in Figure 3.4.

3.5 Slant Column Intensity/Volume Emission Rate Profiles

The profiles in Figure 3.5 represent an altitude/intensity profile because the satellite's camera is viewing along a line of sight in which emissions from various altitudes are viewed. The volume emission rate, VER, profiles can be obtained by taking the altitude/intensity profiles and applying an inversion routine. By using this tool, the altitude where the dayglow reactions are occurring, is obtained. However, in order to perform this inversion process, intensities of the emissions must be obtained.

Since the camera was a broadband camera, it was difficult to calibrate. Jones et al. (1987) found that for aurora the camera has an equivalent 557.7 nm intensity relationship after comparing the Viking data to CANOPUS data, i.e. 14 ± 2 DN are equivalent to 1000 Rayleighs. This relationship was applied to all of the intensity profiles. The results for orbits 1386 99.019 and 1485 99.032 are shown in Figure 3.6.

The altitude/intensity profiles from Figure 3.6 were put into the inversion program (Rochon, 1985). The results of the inversion are shown in Figure 3.7. The VER profile for orbit 1485 has a lower band which is sharp and narrow at an altitude of 115 km. The altitude of the upper band has changed slightly also, from a pre-inversion altitude of 240 km to a post-inversion altitude of 279 km. For 1386, the altitude that the peaks occur at has also changed, from 125 km before the inversion to 150 km after the inversion for the lower peak but the upper peak altitude remains constant at 275 km.

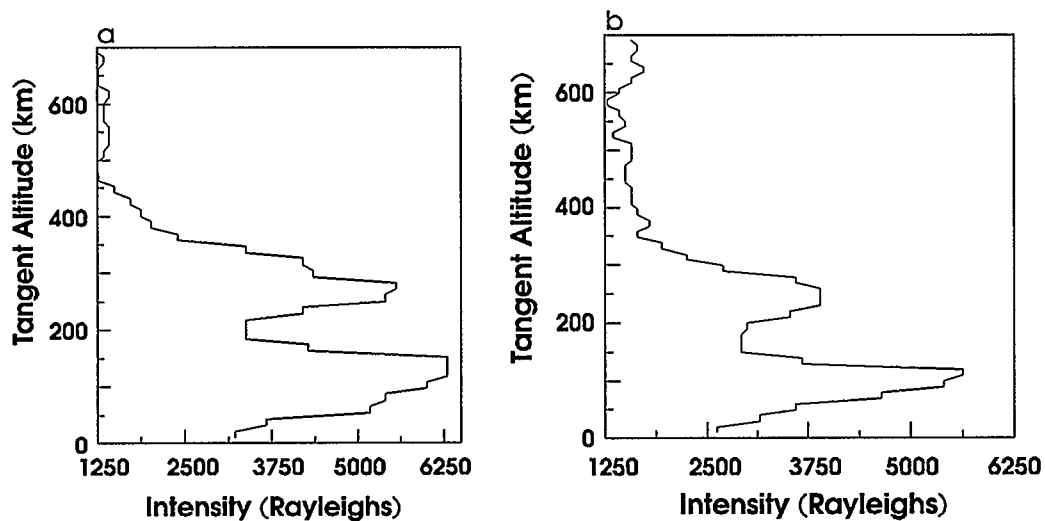


Figure 3.6 Tangent altitude/slant column intensity profiles for
 a) 1386 99.019 b) 1485 99.032

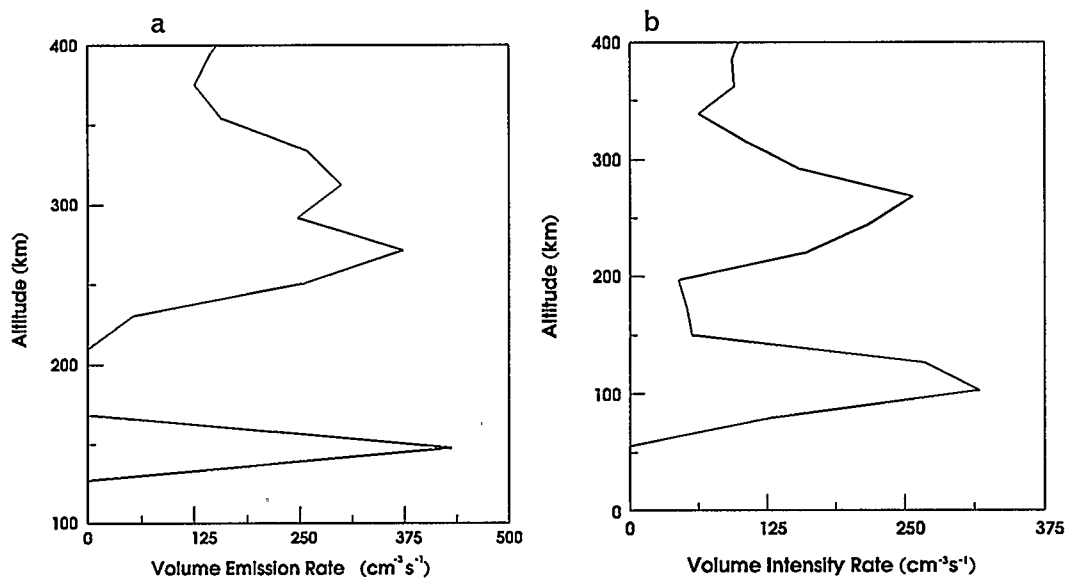


Figure 3.7 Altitude/Volume Emission Rate profiles for
 a) 1386 99.019 b) 1485 99.032

Chapter 4 Model Development

The emissions that are observed by the Viking satellite are caused by electron impact on atoms or molecules (see Table 1.1). The excitation rate of the atmospheric species can be calculated. From this, the volume emission rates of the different species and the column intensities will also be calculated and these results will then be compared to the Viking satellite data.

The volume excitation rate, $j(z)$ ($\text{cm}^{-3}\text{s}^{-1}$), to an atomic or molecular state by photoelectron impact can be calculated from the following equation (Meier, 1991):

$$j(z) = \rho(z) \int_{E_0}^{\infty} \sigma(E)F(z,E)dE = \rho(z)g(z) \quad (4.1)$$

where $\rho(z)$ is the density of the species of interest, $\sigma(E)$ is the electron impact excitation cross-section, $F(z,E)$ is the photoelectron flux ($\text{cm}^{-2}\text{s}^{-1}\text{eV}^{-1}$), and $g(z)$ is the excitation rate. Each one of the above quantities needs to be calculated before the volume rate of emission can be determined.

4.1 Neutral Density, $\rho(z)$

The neutral densities as a function of altitude were obtained using the empirical model of Hedin (1987), the mass spectrometry and incoherent

scatter model, (MSIS-86). The MSIS-86 model is based upon a large number of in-situ measurements from rocket flights, observations from eight satellites (OGO 6, San Marco 3, Aeros A, Atmospheric-C, Atmospheric-D, Atmospheric-E, EROS 4 and Dynamics Explorer B) and data from five incoherent scatter radar stations (Millstone Hill, St. Santin, Arecibo, Jicamarca and Malvern). Spherical harmonic expansions of neutral temperature and neutral species concentrations, N_2 , O_2 , O, Ar, N, H and He, as functions of altitude, geographic location, Universal Time, day of the year and solar and geomagnetic activity are the basis of the model. The solar and geomagnetic activity are specified by the solar microwave flux, $F_{10.7}$, and by the planetary magnetic index, A_p . This data was obtained from the NOAA National Geophysical Data Center CD-ROM data base.

The MSIS model represent the best empirical thermospheric models. Unfortunately, there have been very few measurements between 90 and 150 km. This has resulted in problems in obtaining dependable atomic oxygen profiles, especially during periods of high geomagnetic activity. This has resulted in the "scaling" of atomic oxygen densities by a factor of less than 1 in order to compensate for the uncertainties.

In the model being developed, only the concentrations of N, O, O_2 and N_2 are of interest, since they will directly affect the modelled results. The neutral species densities for both orbits of interest have been calculated. Table 4-1 shows the input parameters for the MSIS-86 program. From the geomagnetic data it can be seen that during these orbits the sun was in a period of low solar activity. The results of this

model calculation are shown in Figure 4.1. From this figure, it can be seen that in both cases the concentrations of N₂, O₂ and O all decrease as the altitude increases. The atomic nitrogen, however, increases, with a maximum concentration at 180 km, and then decreases in concentration.

Table 4-1 Input Data for the MSIS-86 program for Viking Orbits

	Orbit 1386 99.019	Orbit 1485 99.032
Date	86/10/31	86/11/18
Date (yyddd)	86304	86322
Latitude (°N)	53.95	56.81
Longitude (°E)	164.78	178.4
Universal Time (hhmmss)	204522	223334
Local Solar Time	10.40	12.29
Ap	14	6
F _{10.7}	89.8	73.0
3 month average of F _{10.7}	70.67	74.0

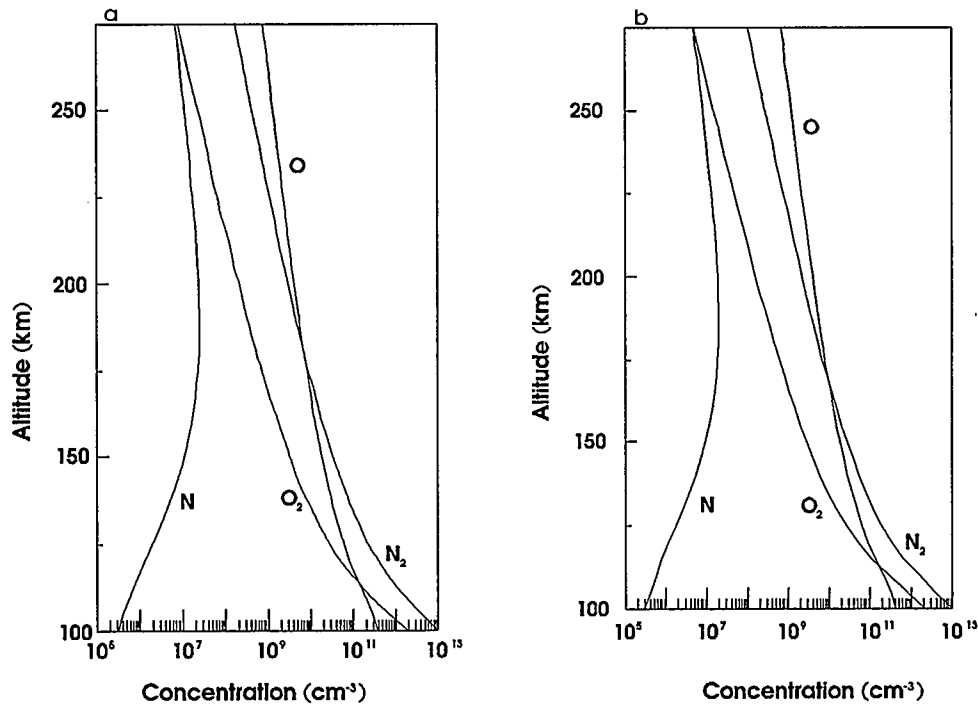


Figure 4.1 Concentrations N, O, O₂ and N₂ as a function of altitude as calculated by the MSIS-86 program for a) 1386 99.019 b) 1485 99.032

4.2 Cross Sections, $\sigma(E)$

The cross section for electron impact is required to calculate the volume emission rate. A cross section for each different atomic or molecular species is required. For the wavelength range covered by the Viking satellite, cross sections for O I 135.6 nm (O I 1356), N I 149.3 nm, N I 174.4 nm and the LBH bands of N₂ are needed. Because the cross section measurements are very difficult to obtain, very few results have been published. To obtain the cross sections required for the model, published plots of $\sigma(E)$ were digitized and the required cross sections were obtained from a cubic spline interpolation of the digitized data..

The emission observed at 149.3 nm for N I atom has a maximum unscaled cross section, as measured by Stone and Zipf (1973), of $3.63 \times 10^{-17} \text{ cm}^2$ occurring at 18 eV. This cross section, however, has been scaled by a factor of 0.7, resulting in a cross section of $2.54 \times 10^{-17} \text{ cm}^2$. The scaling factor has been applied recently to account for the new H₂ L- α calibration standard (Meier 1991).

The emission line at 174.3 nm for N I has an unscaled maximum cross section of $1.3 \times 10^{-17} \text{ cm}^2$ occurring at 17 eV (Stone and Zipf, 1973). The scaling factor of 0.7, again due to the new H₂ L- α calibration standard (Meier 1991), was applied resulting in a scaled cross section of $9.1 \times 10^{-18} \text{ cm}^2$.

The O I 1356 peak has a maximum cross section of $2.5 \times 10^{-17} \text{ cm}^2$ with the peak occurring at 16 eV (Stone and Zipf, 1974). This cross section has a scaling factor of 0.36 applied to it in order to get agreement between the measured cross sections and those determined from dayglow measurements (Conway et al. 1988).

The LBH bands of N₂ have had their cross sections measured by Ajello and Shemansky (1985). The maximum peak cross section was found to be $3.0 \times 10^{-17} \text{ cm}^2$ at 18 eV. No scaling factor had to be applied to this work, but the wavelength range had to be considered. This cross section was for all of the LBH bands, which cover a very large wavelength range. For the region of interest, the branching ratios of the different bands of LBH are multiplied by the total cross section,

resulting in cross sections for each LBH band. The volume emission rate for each one of these bands is calculated and the final VER is the sum of all of the different branches. Table 4-2 shows the 58 different bands, the wavelength that the emission occurs at and their branching ratio for the Viking wavelength region. Figure 4.2 shows all of the cross sectional areas for the four different species as a function of energy.

Table 4-2 LBH Emission Bands of Interest and their Branching Ratios
(Ajello and Shemansky, 1985)

Band	λ (nm)	B.R.	Band	λ (nm)	B.R.	Band	λ (nm)	B.R.
(0,0)	145.0	.00247	(2,7)	176.8	.02125	(5,2)	138.2	.00957
(0,1)	150.1	.00785	(3,0)	135.4	.05832	(5,3)	142.7	.00640
(0,2)	155.5	.01149	(3,1)	139.8	.00354	(5,4)	147.4	.00936
(0,3)	161.2	.01029	(3,2)	144.4	.01969	(5,5)	152.3	.00142
(0,4)	167.2	.00634	(3,3)	149.3	.01605	(5,6)	157.6	.01074
(0,5)	173.6	.00283	(3,4)	154.5	.00088	(5,7)	163.1	.00077
(1,0)	141.6	.01946	(3,5)	160.0	.01824	(5,8)	169.0	.00561
(1,1)	146.4	.02928	(3,6)	165.8	.01070	(5,9)	175.2	.00816
(1,2)	151.5	.01087	(3,7)	171.9	.00008	(6,1)	131.2	.01424
(1,3)	157.0	.00007	(3,8)	178.5	.01144	(6,2)	135.3	.00070
(1,4)	162.7	.00986	(4,0)	132.5	.04854	(6,3)	139.6	.01005
(1,5)	168.8	.08127	(4,1)	136.8	.00171	(6,4)	144.1	.00031
(1,6)	175.2	.01518	(4,2)	141.2	.02392	(6,5)	148.9	.00722
(2,0)	138.4	.04641	(4,3)	145.9	.00010	(6,6)	153.9	.00135
(2,1)	143.0	.02381	(4,4)	150.8	.01579	(6,7)	159.2	.00395
(2,2)	147.9	.00075	(4,5)	156.0	.00644	(6,8)	164.8	.00433
(2,3)	153.0	.02150	(4,6)	161.6	.00310	(6,9)	170.7	.00026
(2,4)	158.5	.01507	(4,7)	167.4	.01423	(6,10)	176.9	.00542
(2,5)	164.2	.00008	(4,8)	173.6	.00427			
(2,6)	170.3	.00979	(5,1)	133.9	.01057			

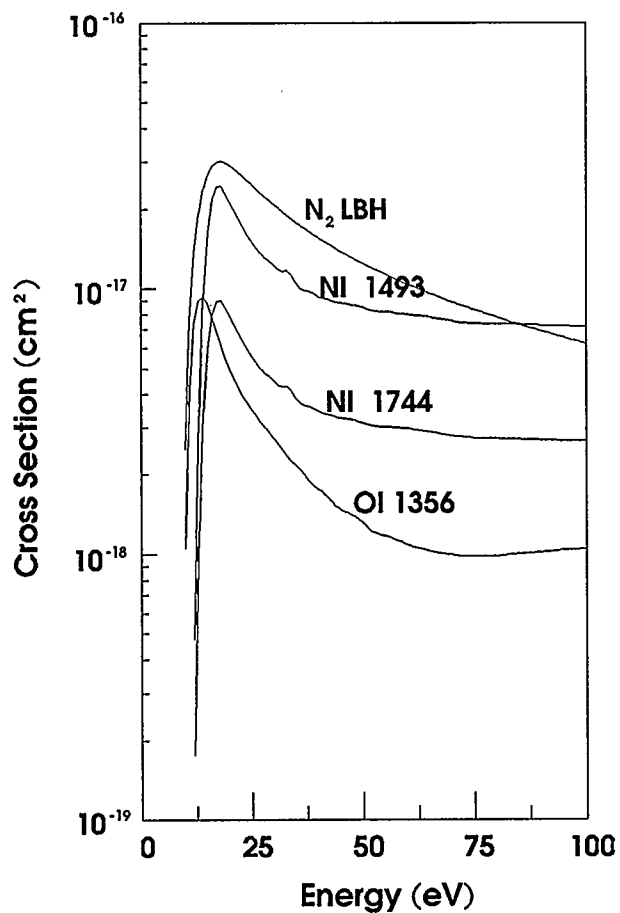


Figure 4.2 Cross sectional area as a function of electron energy

4.3 Photoelectron Flux, $F(z,E)$

A method of calculating the photoelectron flux was needed in order to determine the volume emission rate. A model by Richards and Torr (1983) allows for the calculation of the photoelectron flux as a function of both altitude and energy and requires only a few input parameters. In their model, they have simplified the problem of determining the secondary electron flux. Normally, in other codes, e.g. Strickland and

Meier (1982), the cascading electrons from energy levels above the one being considered produce secondary electrons resulting in very long computation times. If the 1 eV energy level is considered, then not only must the primary production be calculated, but so must the secondary electron contribution for the n other levels above it. Richards and Torr (1983) do not consider the probability of electrons losing from 1 to n eV of energy. They consider an average energy loss at a given energy level and this simplifies the calculation. They have broken the electron energy region into four parts and calculated energy losses for each region.

Another simplification that has been incorporated into the model of Richards and Torr (1983) is cross sectional area. Instead of having to have a knowledge of many different cross sections to calculate secondary electron flux, total inelastic cross sections are used to determine secondary flux. This simplification also greatly decreases computational time.

Richards and Torr compared their model with the full calculations and with AE-E spectra. They found that for altitudes below 300 km, there is good agreement between the simple model, the full model and the measured spectra. Above 300 km, transport processes become important and there are serious differences observed.

The photoelectron flux at energy E has been approximated by Richards and Torr (1983) as:

$$F(z,E) = \frac{(J_o[O] + J_{N_2}[N_2] + J_e[e]) * e^{-\tau} * S_{EUV}}{\sigma_o[O] + \sigma_{N_2}[N_2] + L_{eE}[e]} \quad (4.2)$$

where J_i is the production frequency of species i , $[i]$ is the concentration of species i and τ is the attenuation factor due to the atmosphere, S_{EUV} is the solar cycle attenuation which depends on the magnitude of the solar EUV flux, σ_i is the cross sectional area of species i and L_{eE} is the loss due to thermal electrons.

4.3.1 EUV Flux

In calculating the solar cycle attenuation factor, S_{EUV} , the EUV flux is needed. This is the ratio of the EUV flux for the date and time of interest to a standard EUV flux given by Torr et al. (1979), the solar minimum reference spectrum, SC#21REFW. The solar EUV flux is not a quantity that is measured daily, so a model was needed. The standard EUV flux model that is used is that of Hinteregger et al. (1981).

Unfortunately, it does not cover the time span that Viking was in orbit. The empirical model of Tobiska and Barth (1990) was found to cover the time period in which Viking was in orbit. This model covers from 1981 to 1989 using the EUV data set from Atmosphere Explorer E satellite and 18 separate rocket flights. It covers a wavelength range from 1.9 to 105.0 nm and with the same binning as SC#21REFW.

The input to this model are two measured solar emissions, $F_{10.7}$ and the H Ly- α line at 121.6 nm. While the $F_{10.7}$ data is regularly published,

the H Ly- α data is difficult to find for the time when Viking was collecting data. H Ly- α data from the OSO-5 satellite covers the time period from January 1969 to December 1972 (Vidal-Madjar, 1975) and from August 1974 to August 1975 (Vidal-Madjar and Phissamay, 1980). Data from 1977 to 1980 was collected by the AE-E satellite and from October 1981 until the end of 1988 (Rottman 1988), the Solar Mesosphere Explorer (SME) satellite collected the H Ly- α data (NOAA, 1992). The compilation of this data is shown in Figure 4.3. The period from 1969 to 1974 shows the waning phase of solar cycle 20 with all of solar cycle 21 shown. The time period that Viking was collecting data was during the solar minimum phase of solar cycle 21, resulting in the H Ly- α . values being around 2.5×10^{11} photons $\text{cm}^{-2} \text{s}^{-1}$.

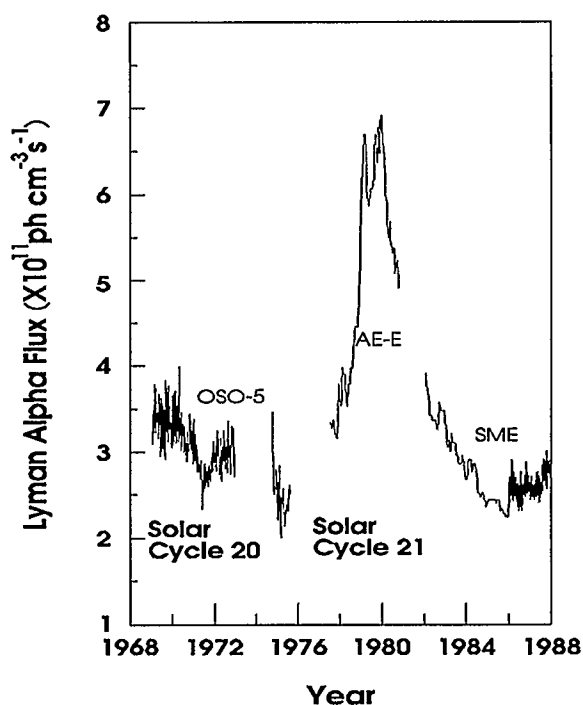


Figure 4.3 The H Ly- α measurements from 1969 to 1988, showing the satellites that collected the data and the Solar Cycles

The ratio of the EUV fluxes calculated by Tobiska and Barth's model to those of SC#21REFW (Torr et al., 1979) are given below in Table 4.3. These ratios are generally less than 1 because the SC#21REFW have been scaled by a factor of two to account for inconsistencies between the measured EUV fluxes and the measured photoelectron fluxes (Richards and Torr, 1983).

Table 4-3 EUV Ratios for Viking Orbits of Study

Wavelength Range (Å)	Orbit 1386 99.019	Orbit 1485 99.032
50-100	0.838	0.764
100-150	1.279	1.187
150-200	0.870	0.785
200-250	1.004	0.822
256.3	0.534	0.534
284.15	2.579	0.903
250-300	2.763	2.062
303.31	0.868	0.528
303.78	0.762	0.762

4.3.2 Electron and Neutral Temperature

Another input that is required in order to calculate the photoelectron flux is the electron and neutral temperatures. The MSIS-86 program (Hedin, 1987) provides the neutral temperatures as a function of altitude.

Two different electron temperature profiles were used in the determination of the photoelectron flux. Normally, at altitudes below 140 km, the electron temperature is set equal to the neutral temperature. However, Duhau and Azpiazu (1985) found that the electrons are not in thermal equilibrium with the neutral species. They determined an empirical relationship for the electron/neutral temperature ratio, which depends on $F_{10.7}$. At altitudes above 140 km, the electron temperature profiles of Rasmussen et al. (1986) were used.

Figure 4.4 shows the electron and neutral temperature as a function of altitude. The electron temperature is much greater than that of the neutral temperature for altitudes above 140 km. Below 140 km, the electron temperature is only slightly higher than the neutral temperature, with the two temperatures merging as the altitude decreases.

4.3.3 Electron Density

The electron density is required in the photoelectron flux calculation in two places, in the production of photoelectrons, i.e. the cascading production due to thermal electron degradation and in the loss due to thermal electrons. To calculate the electron density, the ion chemistry

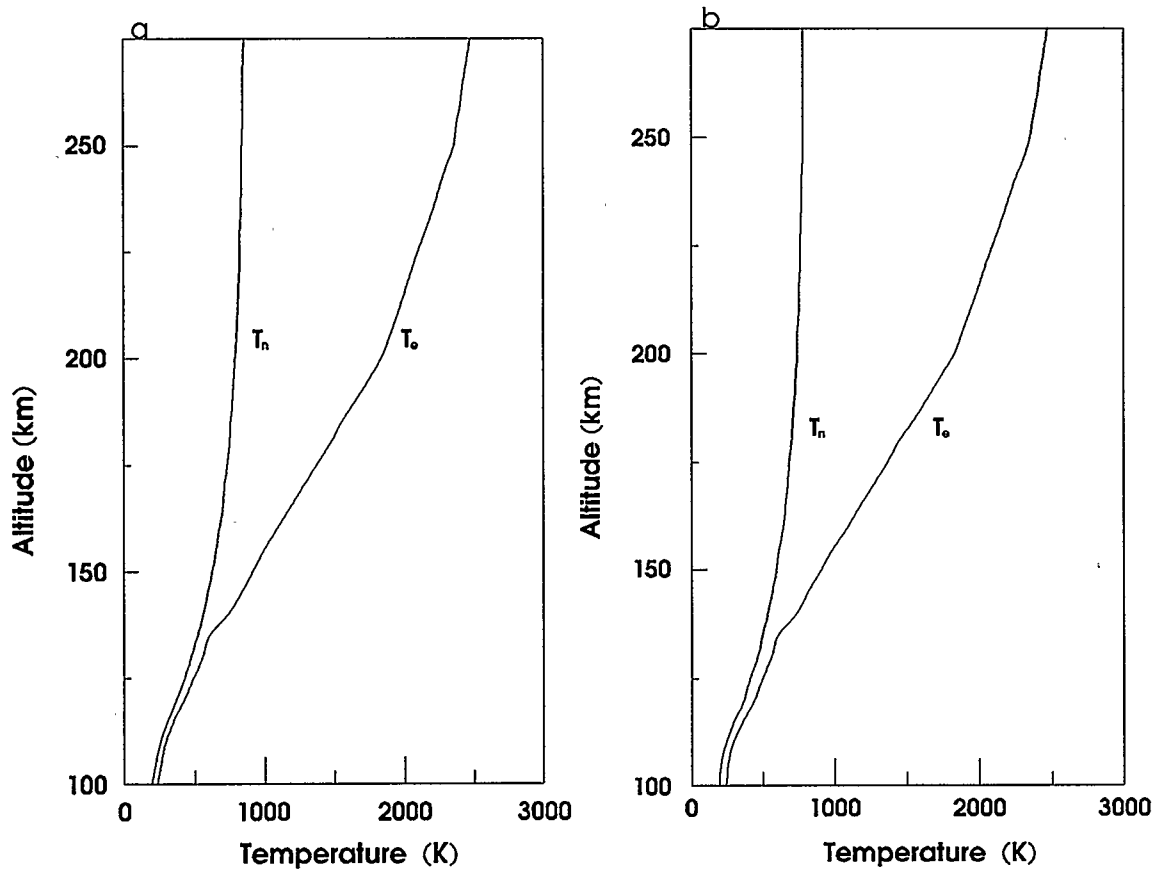


Figure 4.4 The electron and neutral temperatures versus altitude for orbits a) 1386 99.019 b) 1485 99.032

of the ionosphere must be considered. Rasmussen et al. (1988) in modelling the ionospheric conductivity used the rate coefficients of Schunk and Raitt (1980) to determine the electron density. The four most important ions in the ionosphere, N_2^+ , O_2^+ , O^+ and NO^+ , are used to determine the electron density. The altitude profiles of these ions, and thus the electron density profiles, are calculated assuming that photochemical equilibrium occurs. The ion chemical reactions and their rates which are used in the calculations of the electron density are shown in Table 4-4 (Rasmussen et al., 1988; Schunk and Raitt, 1980).

The results of the calculations for both orbits 1386 and 1485 are shown in Figure 4.5, which shows the electron concentration at various altitudes. There is a peak in the electron density at 105 km which is followed by a decrease in the concentration, with a minimum at 135 km. There is then a continuous increase in the electron concentration as the altitude increases.

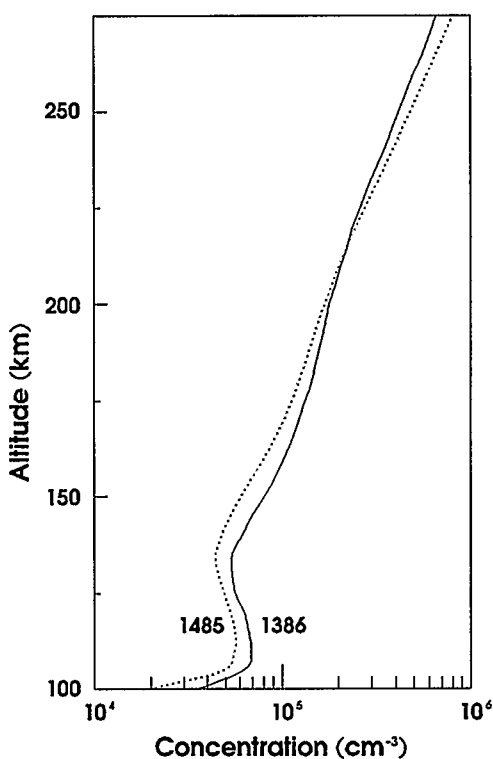


Figure 4.5 Altitude/Electron concentration profiles for orbits 1386 99.019 and 1485 99.032

Table 4-4 Ion Chemical Reactions and Rate Coefficients

Reaction	Reaction Coefficient $\text{cm}^3 \text{s}^{-1}$
$\text{N}_2 + h\nu \rightarrow \text{N}_2^+ + e^-$	
$\text{O}_2 + h\nu \rightarrow \text{O}_2^+ + e^-$	
$\text{O} + h\nu \rightarrow \text{O}^+ + e^-$	
$\text{N}_2^+ + e^- \rightarrow \text{N} + \text{N}$	$1.8 \times 10^{-7} (300/T_e)^{0.39}$
$\text{O}_2^+ + e^- \rightarrow \text{O} + \text{O}$	$1.6 \times 10^{-7} (300/T_e)^{0.55}$
$\text{NO}^+ + e^- \rightarrow \text{N} + \text{O}$	$4.2 \times 10^{-7} (300/T_e)^{0.85}$
$\text{N}_2^+ + \text{O}_2 \rightarrow \text{N}_2 + \text{O}_2^+$	$5 \times 10^{-11} (300/T_e)$
$\text{N}_2^+ + \text{NO} \rightarrow \text{N}_2 + \text{NO}^+$	3.3×10^{-10}
$\text{O}_2^+ + \text{N}_2 \rightarrow \text{NO} + \text{NO}^+$	5.0×10^{-16}
$\text{O}_2^+ + \text{NO} \rightarrow \text{O}_2 + \text{NO}^+$	4.4×10^{-10}
$\text{O}_2^+ + \text{N} \rightarrow \text{O} + \text{NO}^+$	1.2×10^{-10}
$\text{N}_2^+ + \text{O} \rightarrow \text{N} + \text{NO}^+$	$1.4 \times 10^{-10} (300/T_e)^{0.44}; T \leq 1500 \text{ K}$ $5.2 \times 10^{-11} (300/T_e)^{0.2}; T > 1500 \text{ K}$
$\text{N}_2^+ + \text{O} \rightarrow \text{N}_2 + \text{O}^+$	$1.0 \times 10^{-11} (300/T_e)^{0.23}; T \leq 1500 \text{ K}$ $3.6 \times 10^{-12} (300/T_e)^{0.41}; T > 1500 \text{ K}$
$\text{O}^+ + \text{N}_2 \rightarrow \text{N} + \text{NO}^+$	$1.533 \times 10^{-12} - 5.92 \times 10^{-13} (T/300) + 8.60 \times 10^{-14} (T/300)^2$ $300 \leq T \leq 1500 \text{ K}$ $2.73 \times 10^{-12} - 1.155 \times 10^{-12} (T/300) + 1.483 \times 10^{-13} (T/300)^2$ $1700 < T < 6000 \text{ K}$
$\text{O}^+ + \text{O}_2 \rightarrow \text{O} + \text{O}_2^+$	$2.82 \times 10^{-11} - 7.74 \times 10^{-12} (T/300) + 1.073 \times 10^{-12} (T/300)^2$ $- 5.17 \times 10^{-14} (T/300)^3 + 9.65 \times 10^{-16} (T/300)^4$ $300 \leq T \leq 6000 \text{ K}$
$\text{O}^+ + \text{NO} \rightarrow \text{O} + \text{NO}^+$	$8.36 \times 10^{-13} - 2.02 \times 10^{-13} (T/300) + 6.95 \times 10^{-14} (T/300)^2$ $320 \leq T \leq 1500 \text{ K}$ $5.33 \times 10^{-13} - 1.64 \times 10^{-14} (T/300) - 4.72 \times 10^{-14} (T/300)^2$ $- 7.05 \times 10^{-16} (T/300)^3; 1500 < T < 6000 \text{ K}$

4.3.4 Photoelectron Flux

With the temperature, EUV flux and the electron density calculated, the photoelectron flux can be calculated using the model of Richards and Torr (1983). The photoelectron flux at various altitudes is required in order to calculate the volume emission rates. Figure 4.6 shows the results of the model calculations for both orbits at various altitudes. From these figures, it can be seen that the photoelectron flux increases as the altitude increases. This is to be expected since the number of photoelectrons quenched will decrease as the altitude increases due to the decreased concentration of all species.

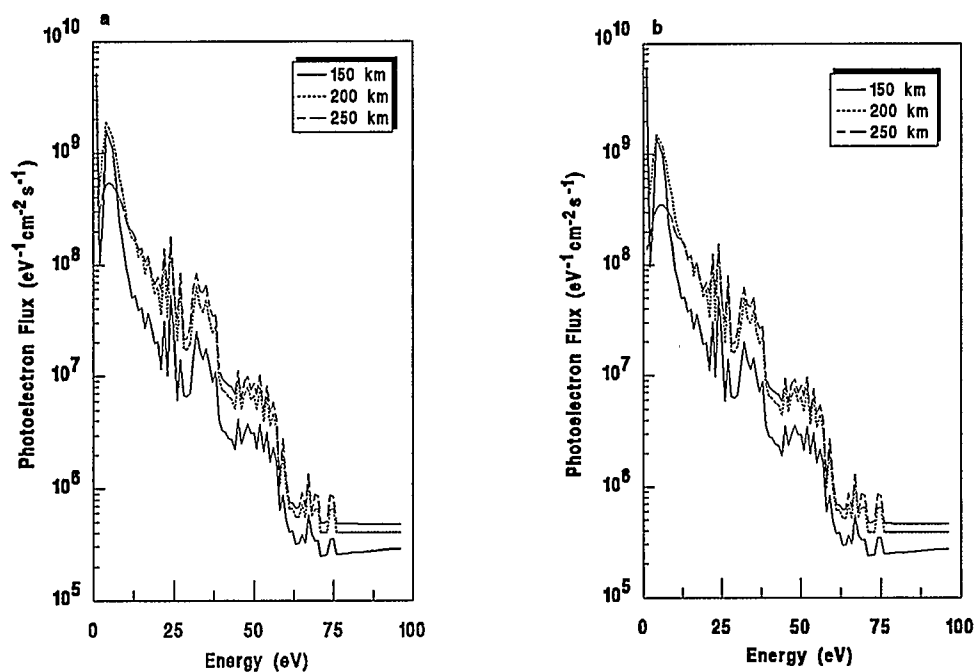


Figure 4.6 The calculated photoelectron flux as a function of energy for Viking orbits a) 1386 99.019 b) 1485 99.032

4.4 Schumann-Runge Bands

The Schumann-Runge absorption bands of O_2 quench emissions from both LBH and $O\ I\ 1356$. The SR continuum causes an absorption of the LBH bands in the lower thermosphere. (Strickland et al., 1983). This decreases the number of lines contributing to the emission at a given altitude, resulting in a decrease in the VER. Figure 4.7 shows the auroral spectrum and the O_2 absorption cross section, i.e. the altitude at which a line is absorbed. Also shown on the vertical axis is the altitude of O_2 absorption, i.e. the altitude at which the bands will be 100% absorbed (Strickland et al., 1983).

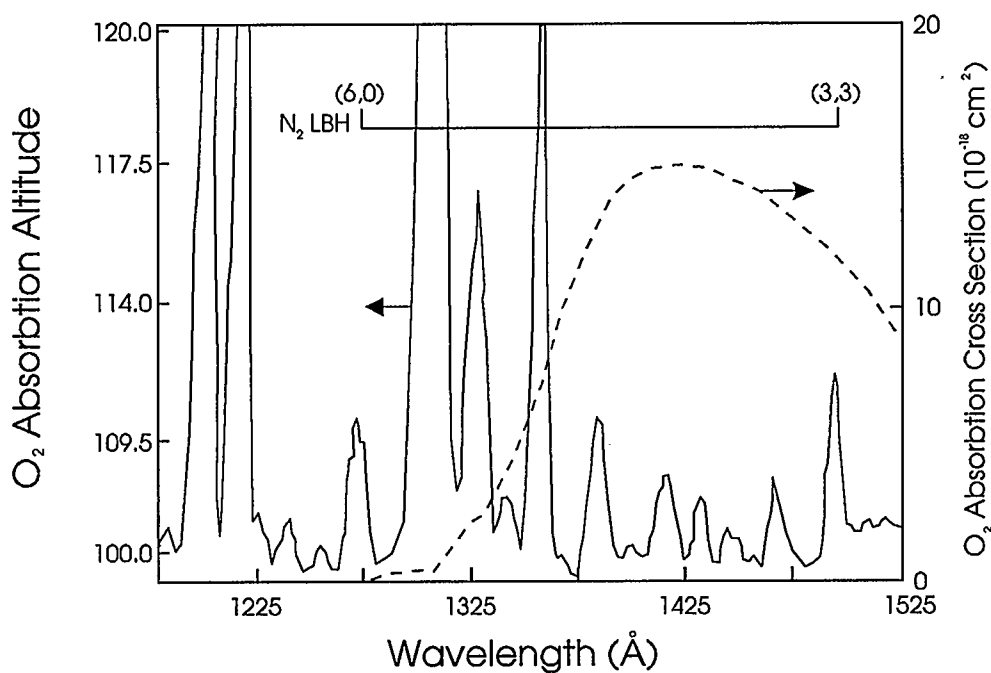


Figure 4.7 Schumann-Runge O_2 absorption cross section and altitude of O_2 absorption of LBH lines

Table 4-5 LBH branching ratios at different altitudes due to Schumann-Runge Absorption

Altitude (km)	LBH Bands Emitting	Total LBH Branching Ratio
100	(0,3)(0,4)(0,5)(1,3)(1,4)(1,5)(1,6)(2,4)(2,5) (2,6)(2,7)(3,5)(3,6)(3,7)(3,8)(4,6)(4,7)(4,8) (5,7)(5,8)(5,9)(6,0)(6,1)(6,7)(6,8)(6,9)(6,10)	0.229
105	100 km bands + (4,0)(5,6)	0.289
110	105 km bands + (6,6)(3,4)(0,2)(4,5)(5,1)(6,2)	0.320
115	110 km bands+ (3,0)(2,3)(4,1)(0,1)(1,2)(4,4)(5,5)(3,3)(6,5)(5,2)	0.472
120	115 km bands + (2,0)(3,1)(6,3)(1,0)(4,2) (5,3)(2,1)(6,4)(5,2)(0,0)(4,3)(1,1)(5,4)(2,2)	0.696

For wavelengths longer than 152.5 nm, the altitude of O₂ absorption has been extrapolated. Table 4-5 shows the bands which are emitting as well as the new total branching ratio for LBH (Ajello and Shemansky, 1985) at that altitude. From the table, it can be seen that the Schumann-Runge bands decrease the total branching ratio from 0.696 at altitudes above 120 km to 0.229 at 100 km, a significant decrease.

4.5 Volume Emission Rates

With methods for determining the neutral concentration, the excitation cross sectional areas and the photoelectron flux, the volume emission rates can be calculated. Equation (4.1) is used to calculate the volume emission rate at a given altitude:

$$j(z) = \rho(z) \int_{E_0}^{\infty} \sigma(E) F(z, E) dE = \rho(z) g(z) \quad (4.1)$$

To integrate the above equation, a cubic spline numerical integration technique is used. This is the best technique for situations where the functions to be integrated are tables of numbers and where the interval size is non uniform (Gerald and Wheatley, 1990).

The VER for each LBH line is calculated, with the final VER being the sum of each individual VER. Figure 4.8 shows the VER for all of the lines of interest for both orbits 1386 and 1485. From this figure, it can be seen that the two N I lines do not contribute much to the total VER. The N I VER is at least two orders of magnitude less than the O I 1356 and the LBH contribution. The O I 1356 VER becomes greater than the LBH VER at an altitude of between 235 to 240 km for orbit 1386 and at an altitude of between 220 to 225 km for orbit 1485. The maximum total VER occurs at altitudes of 150 km and 145 km for orbits 1386 99.019 and 1485 99.032 respectively.

4.6 Slant Column Intensity

The cameras on satellites and rockets do not measure the volume emission rate, but rather a column intensity. The column intensity, CI, is calculated by integrating the volume emission rates along the line of sight, which can be expressed as:

$$4\pi I = \int g(z)\rho(z)ds \quad (4.3)$$

where $4\pi I$ is the intensity of the emission measured in Rayleighs, 10^6 photons $\text{cm}^{-2} \text{s}^{-1}$.

The satellite cameras view the emissions from outside the emission regions. Thus they are not viewing a vertical column of atmosphere, but rather a slant column of atmosphere. From each layer the light travels along the line of sight to the camera. The distance between the different layers along the line of sight changes, since the earth is round, resulting in different integration intervals and possible changes in the solar zenith

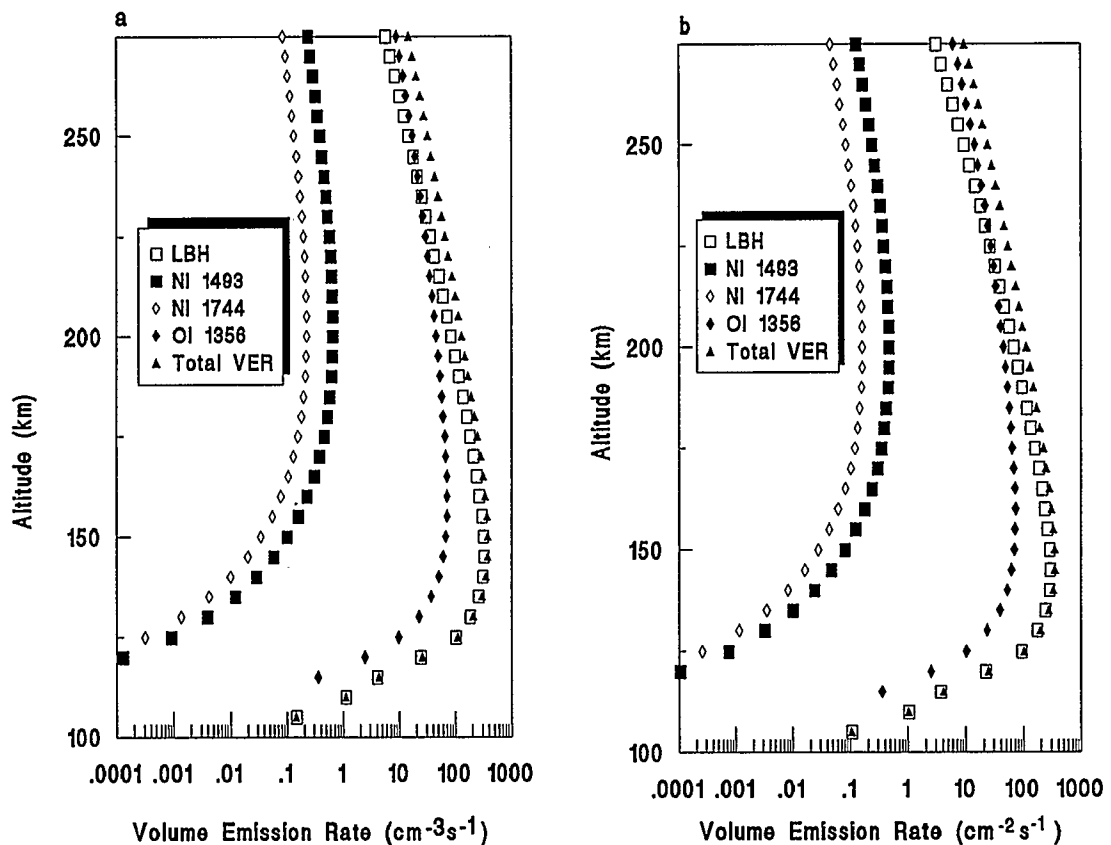


Figure 4.8 Volume emission rate at various altitudes for orbits

a) 1386 99.019 b) 1485 99.032

angle. Also, it must be remembered that the emissions come not only from the layers of the atmosphere closest to the satellite, but from those on the far side of the column of interest (see Figure 3.1). The emissions from the far side of the column of interest may also be attenuated due to absorption by the Schumann-Runge bands as the light travels from the far side to the satellite.

The simplest calculation is to assume that the solar zenith angle does not change along the line of sight, resulting in no changes in the neutral densities or the photoelectron flux. Figure 4.9 shows the results of such a calculation. This figure shows that for orbit 1386 the maximum intensity for the LBH bands occurs at 135 km with the O I 1356 maximum occurring at 145 km. The maximum for the total intensity is at 135 km. It should be noted that at 225 km the O I 1356 intensity becomes larger than the LBH intensity. For orbit 1485, the maximum intensities occur at the same altitudes as for 1386, 145 km for the maximum O I 1356 intensity and 135 km for the LBH and the total intensity. In this case, the intensity of the O I exceeds that of the LBH at 210 km. The intensities at lower altitudes are not as large as those at higher altitudes due to quenching of the emissions by O₂. The general shape of these profiles, and the intensities, are very similar to those calculated by Meier (1991).

A detailed calculation of the intensity would account for the change in the solar zenith angle and geographic location, since these changes will effect the photoelectron flux, the neutral concentrations and the

electron density. The Viking data base has associated with it an interactive processing system, xsystem, which allows for the reading, processing, and displaying of the Viking data. One of the functions, time, gives geographic position information of the satellite. Using this system, the satellite location and altitude was found and the distance along the line of sight from the satellite to the column of interest and the angle formed between the satellite, center of the earth and the column of interest were calculated using the Law of Cosines and Sine's and the results are shown in Table 4-6.

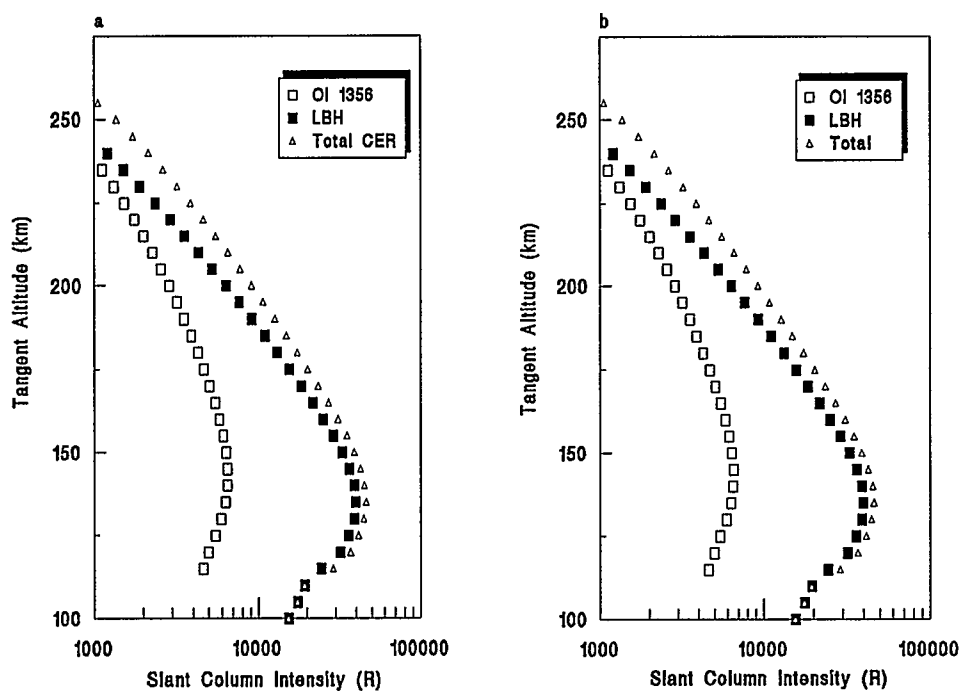


Figure 4.9 Tangent altitude/slant column intensity profiles for
a) 1386 99.019 b) 1485 99.032

Table 4-6 Satellite Parameters used in Calculating Column Intensity.

	1386 99.019	1485 99.032
Satellite Longitude	30.65°	18.00°
Satellite Latitude	71.58°	71.18°
Satellite Altitude from Surface	3944 km	3177 km
Line of Sight Distance	7942 km	7471 km
Angle between satellite, center of earth and column 235	50.30°	51.17°
Change in latitude from initial position to ground location of last emitting layer of atmosphere	2.9°	2.5°

From the initial position, the great circle distance to the last layer's geographic position was determined and the latitude and longitude of this position was also found from the Law of Sines. Table 4-6 shows the change in latitude, and this small change, less than three degrees, results in the same change in the solar zenith angle, allowing the simple model for calculation of slant column intensity to be used, as shown in Figure 4.9.

4.7 Column Intensity

In Figure 4.10, the calculated altitude/column intensity profiles that might be measured by a rocket are shown. In this case, the emissions are much less than for the satellite case since the atmosphere that the

rocket views is only half that a satellite views. The maximum intensity occurs at 135 km for the LBH emission and at 145 km for O I 1356. Also, the intensity of O I 1356 exceeds the LBH emission at 205 km. Also, below 120 km the intensity decreases very quickly, due to the absorption of bands by molecular oxygen. The O I 1356 is completely absorbed by O₂ below 115 km. The emissions from the altitudes above the altitude of interest may be absorbed by the oxygen as it travels to the rocket, e.g. the emission from LBH traveling from the 240 km layer will be partially quenched due to O₂ when observed by the rocket at 110 km. These profiles are similar to those calculated by Meier (1991).

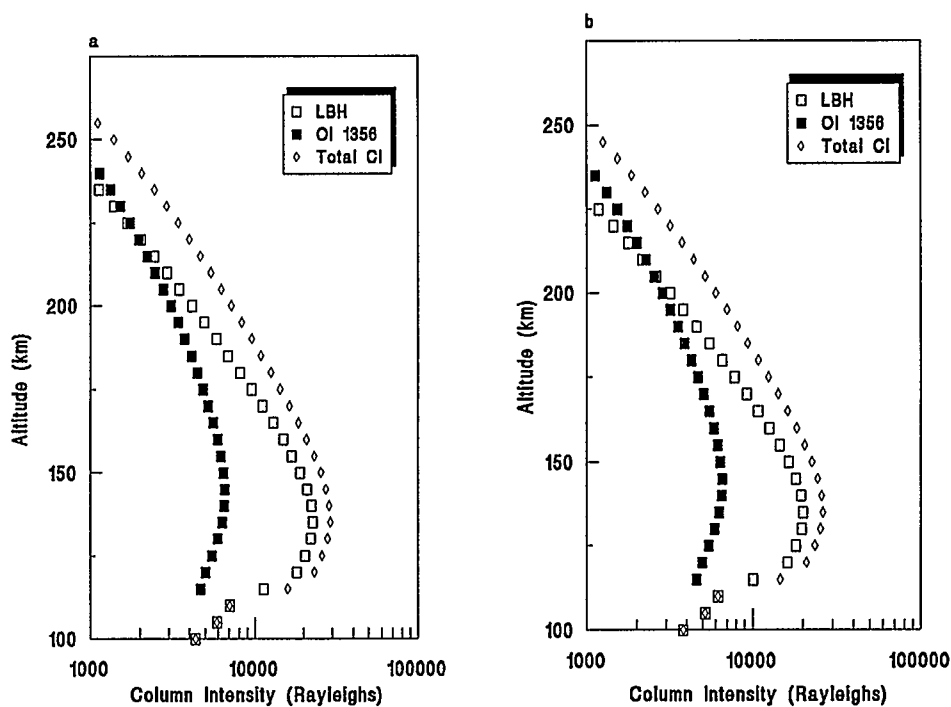


Figure 4.10 Modelled altitude/column intensity profiles as seen by a rocket for a) Orbit 1386 b) Orbit 1485

Chapter 5 Discussion

The results of the model and the inversion routine are compared to those in the literature. The results are examined in two different ways, first is to examine the difference with the solar cycle, at solar minimum and solar maximum and the second is comparison of the model to those that appear in the literature.

5.1 Modelled Results

5.1.1 Neutral Composition and Temperature Profiles

The changes in solar activity affect the photoelectron flux and the concentration of the different species which affects the CI that the satellite or rocket will view. Table 5-1 shows the parameters that were used for the low and high solar activity calculations. Figure 5.1 shows the neutral concentrations for both the solar minimum and maximum periods. From this it can be seen that the concentration of the neutrals is higher for the solar maximum case than for the minimum. Further, the difference between the concentration of a species increases as the altitude increases. For atomic nitrogen, the altitude of the maximum concentration increases from 185 km at solar minimum to 195 km at solar maximum. Figure 5.2 shows that the neutral temperature/altitude profile follows the same trend as the neutral concentration, i.e. the

Table 5-1 Parameters Used in Model Calculations for Solar Minimum and Maximum Conditions

Parameter	Solar Minimum	Solar Maximum
Date	Oct. 31, 1986	Oct. 31, 1980
Latitude	53.95°	53.95°
Longitude	164.78°	164.78°
Local Solar Time	10.4	10.4
F _{10.7}	89.8	212.6
3 month average F _{10.7}	70.67	200.5
A _e	62	565
A _p	14	30
Ly-α	2.75 X 10 ¹¹	5.40 X 10 ¹¹

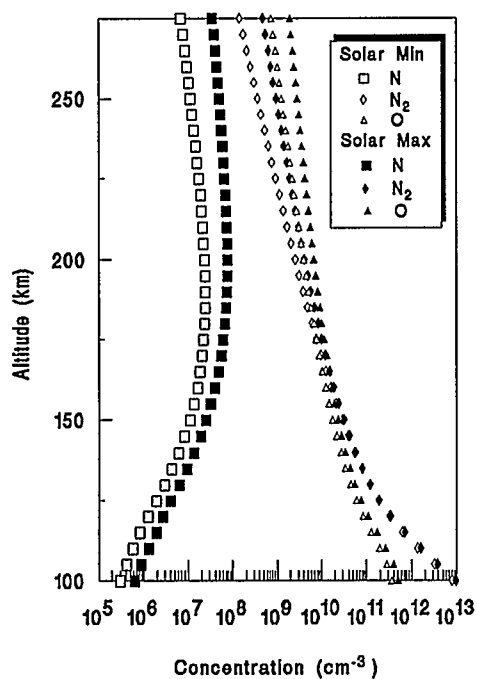


Figure 5.1 Atmospheric concentrations from the MSIS-86 model at solar minimum and solar maximum

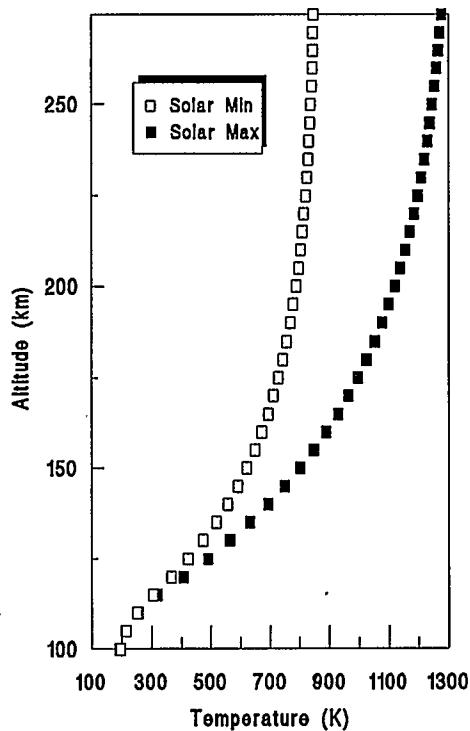


Figure 5.2 Neutral atmospheric temperatures from the MSIS-86 model at solar minimum and maximum

electron temperature for the solar maximum is greater than the solar minimum case. This increase is due to the greater solar UV radiation heating rates at solar maximum (Rees, 1989).

5.1.2 Photoelectron Flux

The photoelectron flux also changes with the solar activity. Figure 5.3 shows the photoelectron flux at two altitudes for both solar minimum and solar maximum. For photoelectrons at an altitude of 150 km, the photoelectron flux at an energy below 25 eV is the same for solar minimum and solar maximum. The flux is much less due to the denser atmosphere. At higher altitudes, the atmospheric density is much less

than at lower altitudes, by orders of magnitude, and so the flux of photoelectrons are not quenched to the same extent. The difference in the photoelectron flux and in the neutral density results in a change in the volume emission rates. At solar minimum the VER is lower than at solar maximum, as shown in Figure 5.4.

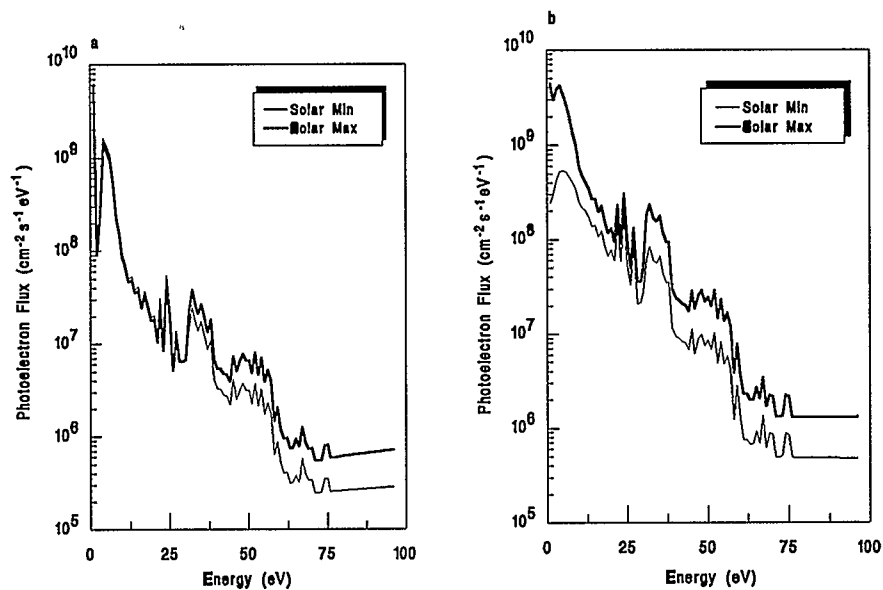


Figure 5.3 Photoelectron flux versus energy for solar minimum and solar maximum at a) 150 km b) 250 km

5.1.3 Volume Emission Rate

Figure 5.4 shows that the peak altitude for the VER for the LBH emissions increases from 145 km to 150 km in going from solar minimum to maximum. In the case of the O I 1356 VER, the peak altitude increases from 160 km to 170 km. This increase is probably due to the change in the neutral concentration profile and the temperature profile. In figure 5.4 for the solar maximum case, the VER

begins to increase above an altitude of 250 km. This increase is an artifact of the photoelectron flux model that was used. In this model the transport processes are not considered, which is important in the solar maximum conditions. In the solar minimum case, the transport does not significantly affect the photoelectron flux at the higher altitudes.

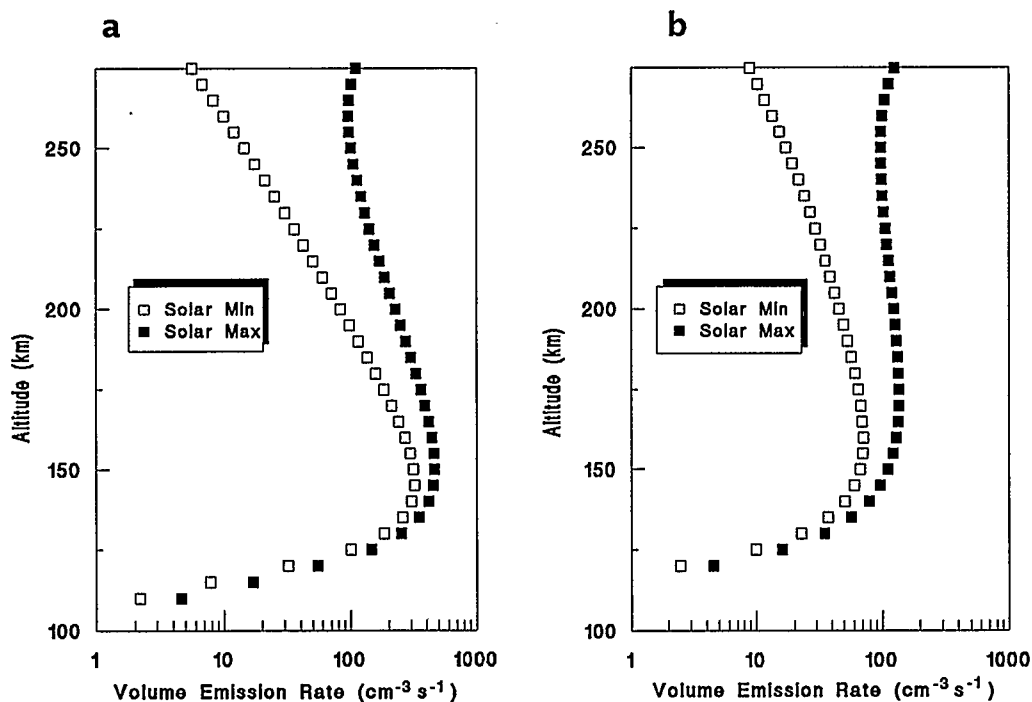


Figure 5.4 Volume emission rates at different altitudes at solar minimum and solar maximum for a) LBH bands b) O I 1356

5.1.4 Column Intensity

Figure 5.5 shows the tangent altitude/slant column intensity for the O I 1356 and the LBH bands that might be observed by a satellite. The

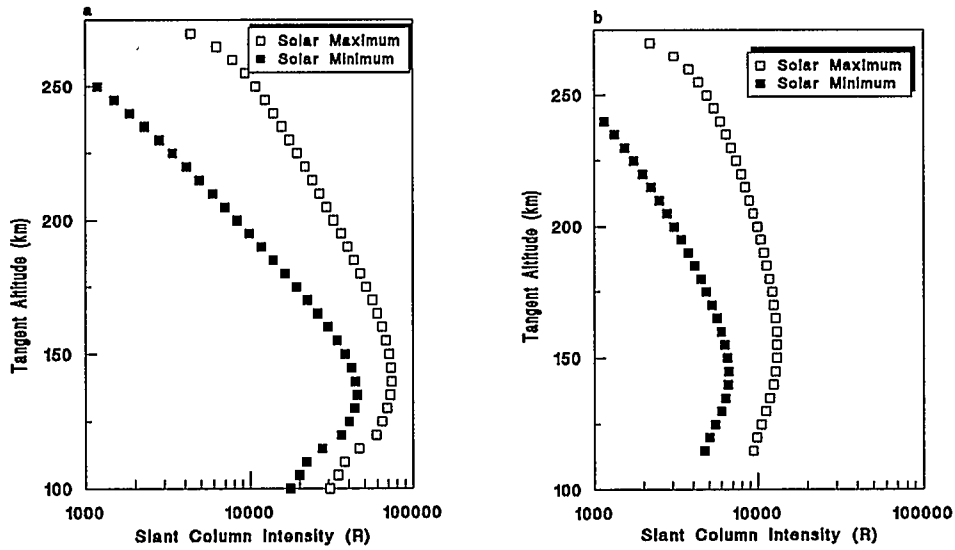


Figure 5.5 Tangent altitude/Slant column intensity profiles for
 a) Lyman-Birge-Hopfield Bands b) O I 1356 as viewed by a satellite

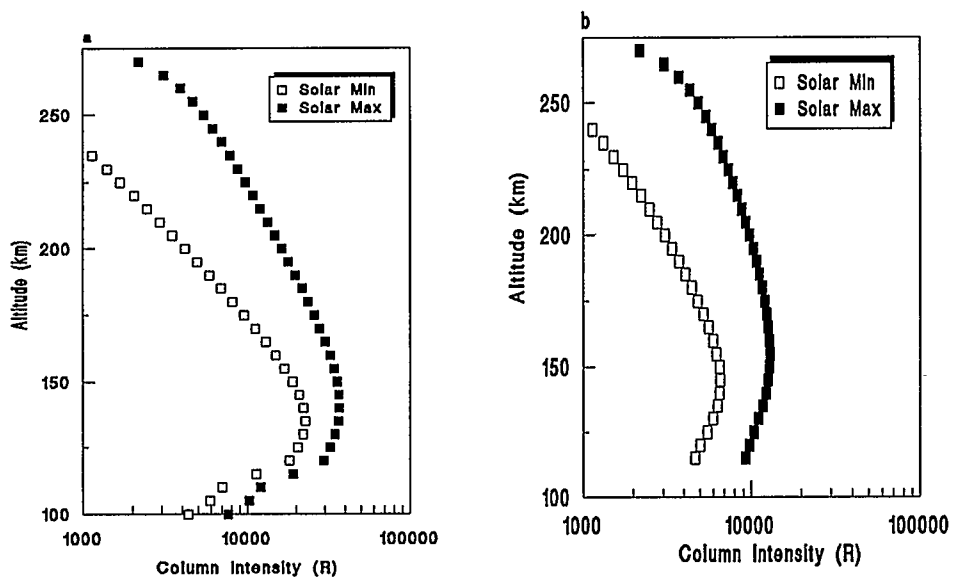


Figure 5.6 Altitude/Intensity profiles for a) Lyman-Birge-Hopfield Bands
 b) O I 1356 as viewed by a rocket

maximum CI occurs at an altitude of 145 km for O I 1356 for both the solar minimum and solar maximum cases. In the case of LBH, the maximum CI occurs at 135 km for solar minimum and 140 km for solar maximum. In the LBH case, the CI decreases drastically below 120 km. This great decrease is due to the SR absorption. For O I 1356, the SR absorption of the emission is nearly complete below 120 km, and there is no emission. For O I 1356, the CI in solar maximum is three times larger than at solar minimum. The LBH CI at solar maximum is twice that at solar minimum. These two profiles are similar to the profiles calculated by Meier (1991).

Figure 5.7 shows the change in CI as viewed by a rocket at solar maximum and solar minimum. For the LBH bands, the maximum intensity at solar minimum occurs at 135 km and at 145 km at solar maximum. Below an altitude of 120 km the slope of the curves change, due to absorption of the LBH emissions by O₂. The CI for O I 1356 is shown in Figure 5.6b with a maximum intensity at 140 km at solar minimum and 150 km at solar maximum. This profile is again similar to the profiles that have been calculated by Meier (1991).

5.2 Comparison of Modelled Results to Published Results

5.2.1 Photoelectron Flux

The simple model of photoelectron flux (Richards and Torr, 1983) is the simplest of the photoelectron flux models that are in use. Two other models of photoelectron flux, those of Link et al. (1988) and Strickland

and Meier (1982) are much more complicated. For example, the model of Link et al. (1988) incorporates energy dependent angular scattering phase functions. It also includes radiative transfer of the 135.6, 130.4 and 98.9 nm multiplets of O I and includes corrections for temperature variations in the atmosphere. The model of Strickland and Meier (1982) includes a detailed solar irradiance spectrum.

Figure 5.7 shows a comparison of the simple model of Richards and Torr (1983), Link et al. (1988) and Strickland and Meier (1982) at an altitude of 170 km. The parameters relevant to the calculation of the photoelectron flux are shown in Table 5-2. The models of Link et al. (1988) and Meier et al. (1982) show close agreement to 60 eV and diverge above 60 eV. The model of Richards and Torr (1983) gives results which are close to the other two models to 30 eV. Above 30 eV, the simple model photoelectron fluxes are approximately a factor of 2 larger than those from the other two models.

The difference between the simple model and the other models may be due to several factors. The model was developed based on AE-E photoelectron spectra. The main difference occurs in the calculation of the secondary photoelectron flux. The more complete codes of Link et al. (1988) and Strickland and Meier (1982) perform detailed calculations on this production whereas the simple model does not perform this calculation (see Chapter 4.3).

There are also some other factors that may affect the shape of the spectra. These spectra were collected in December, 1975 and January

Table 5-2 Geophysical Parameters Relevant to the 1978 Photoelectron Flux Calculation

Date	Jan. 9, 1978
Local Time	1300 MST
Latitude ($^{\circ}$ N)	32.4 $^{\circ}$
Longitude ($^{\circ}$ W)	106.3
$F_{10.7}$	106.3
3 month Average $F_{10.7}$	115.9
A_p	23
A_e	63
Ly- α	3.54×10^{11}

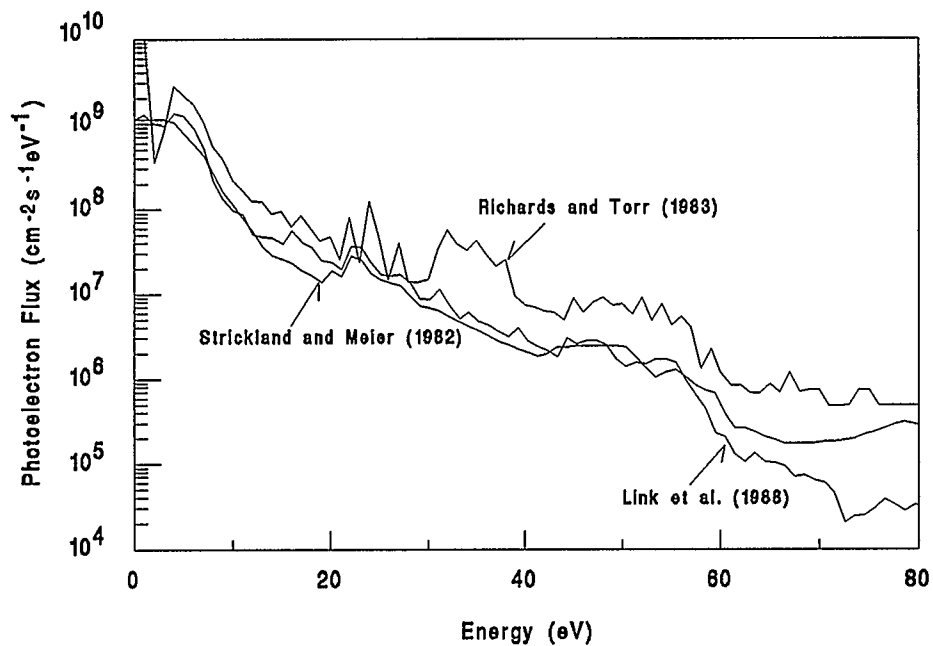


Figure 5.7 Comparison between different photoelectron flux models for an altitude of 170 km

1976, during a solar minimum. The flux that was calculated was for January, 1978, a period of increasing solar activity. The constants used in the photoelectron flux calculation may need to be corrected to allow for the increasing solar activity. A second source of error may occur in the solar EUV flux calculation. The solar EUV flux model of Tobiska and Barth (1990), is valid from 1981 to 1989. The variation of the EUV flux model outside this period is not known, and this variation may have effected the photoelectron flux calculation. The variations observed in the simple model of calculating the photoelectron flux are not uncommon. Variations by factors of two are commonly observed and are attributed to a lack of measured spectra and in solar EUV flux spectral irradiance (Meier, 1991).

5.2.2 Column Intensity

Nearly all of the published results on LBH dayglow examine a monochromatic line, (see Chapter 2). To compare results from the model developed to previously published results, the code was modified to give CI for a specific band of the LBH region. Link et al. (1988) have examined O I 1356 and LBH data that was collected from a rocket flight in 1980 over White Sands. The rocket contained three spectrometers, one which covered the EUV region, 53-125 nm, the second covered the FUV region, 108-150 nm, both with a spectral resolution of 0.35 nm. and a third which covered 129.5-132 nm with a resolution of 0.11 nm. This flight corresponded to relatively active solar conditions, as seen in Table 5-3.

Table 5-3 Geophysical Parameters for the 1980 Rocket flight

Launch Date	June 27, 1980
Local Time	1300 MDT
Latitude (°N)	32.4
Longitude (°W)	106.3
$F_{10.7}$	212.6
3 month average $F_{10.7}$	200.5
A_p	3
A_e	32
$Ly-\alpha$	5.402×10^{11}

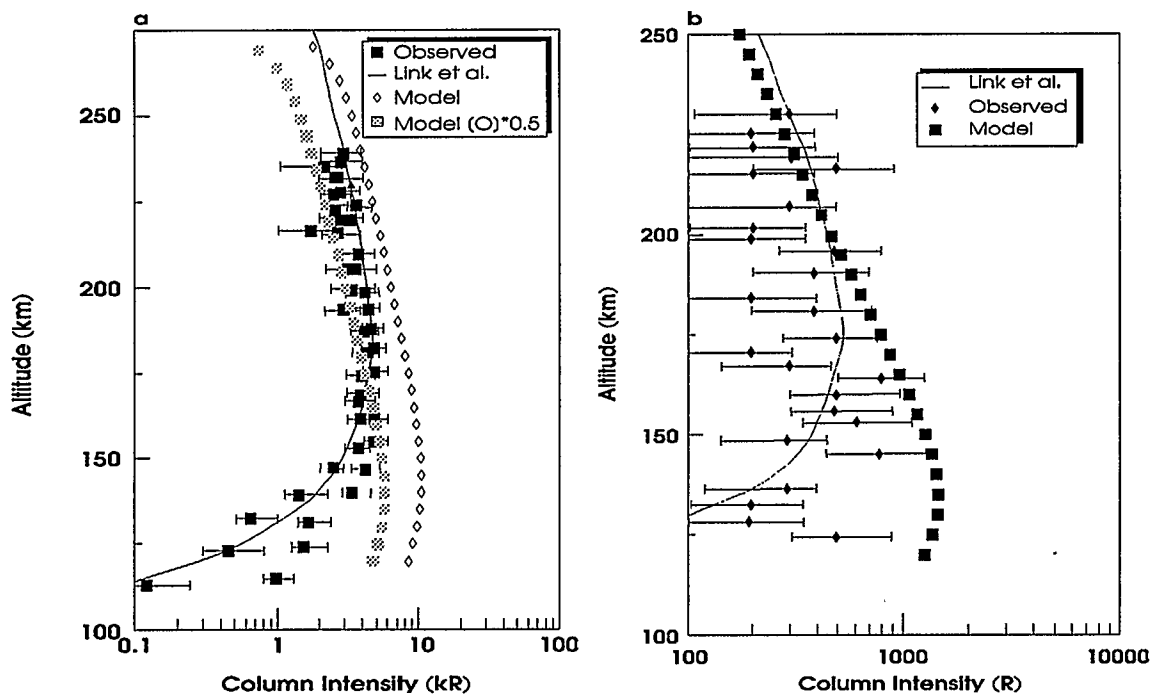


Figure 5.8 A comparison of results from this Model, the Model of Link et al. (1988) and 1980 Rocket Results for a) O I at 135.6 nm b) LBH band at

144.5 nm

This data was used to model the O I 1356 and the LBH band at 144.5 nm. The results from the modelling are compared in Figure 5.8 to the data collected from the rocket and to the model results of Link et al. (1988).

The results from the model are generally higher by a factor of two when compared to the results from Link et al. (1988). The O I 1356 modelled results are higher than the data obtained by the rocket and the results of the model of Link et al. (1988). When the concentration of atomic oxygen in the model is decreased by a factor of two, the results from this model are similar to the other results down to an altitude of 140 km. This type of adjustment in the atomic oxygen is common, e.g. Meier et al. (1985), due to uncertainties in the modelled MSIS-86 atomic oxygen.

There is a difference between the data, the model of Link et al. (1988) and this model below 140 km. A major cause for this difference is the absorption of the emissions by O₂, the Schumann-Runge bands. The O₂ absorption coefficients used in the model, from Strickland et al. (1983), are valid below 120 km. These values may not be large enough and may not extend high enough into the atmosphere.

Figure 5.8b shows a comparison for the LBH band at 144.5 nm. The modelled data, the model of Link et al. (1988) and the rocket data all agree to an altitude of 160 km. Below this altitude the modelled data diverges from the model of Link et al. (1988) but continues to agree with the rocket data to 145 km. In this case, cutting the N₂

concentration in half does not give better agreement between the data and the model.

The divergence between the different models is probably caused by the Schumann-Runge bands of O_2 , and not due to self absorption. Conway (1982) examined the self absorption of N_2 and found that the intensity of the (4,0) band of N_2 is greatly decreased below 150 km due to O_2 absorption, but hardly any decrease was noticed due to N_2 self absorption. Again, the O_2 absorption factor that has been used in the model (Strickland et al., 1983) does not appear to be large enough.

5.3 Viking Data Results

5.3.1 Comparison of the Volume Emission Rate Profiles

The analysis of the Viking data discovered that there are two peaks, one at 120 km and the other above 240 km. These peaks do not match the observations of other authors, e.g. Meier et al. (1985). In their work, only one peak was observed. It should be recalled that their work was conducted using rockets, not satellites, which has an effect on the results.

To try and obtain a correlation between the Viking data and the model, the observed altitude/intensity profile was adjusted. The first peak was adjusted so that the altitude of the second peak corresponds with the results obtained by the model. The altitude in the altitude/intensity

profile was adjusted to 145 km on both orbits. This profile was then inverted using the inversion program of Rochon (1985) and the resulting altitude/VER profiles are shown in Figure 5.9.

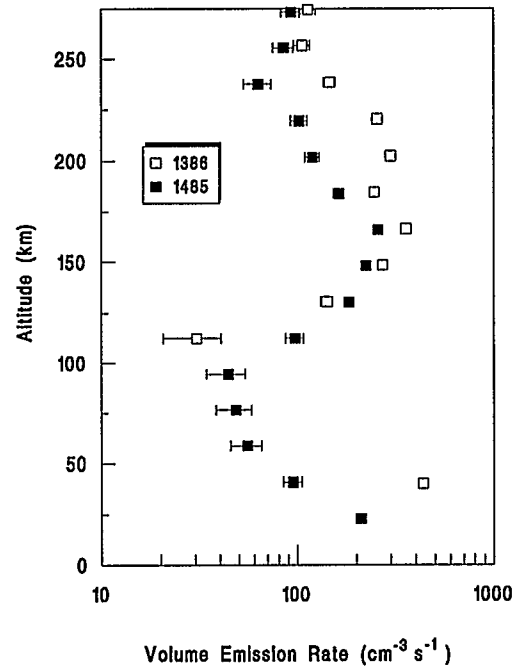


Figure 5.9 Adjusted altitude/VER profiles for orbits 1386 99.019 and 1485 99.032

From this figure, the maximum emission occurs at 165 km for orbit 1485 and at 165 km for orbit 1386. Below 100 km there is an increase in the VER. This increase below 100 km is not observed in the model calculations. This increase in the VER could be caused by unknown tropospheric processes.

Figure 5.10 shows a comparison of the model VER for orbits 1386 99.032 and 1485 99.032 to those obtained from the Viking satellite. The inverted profile peaks are very similar to the modelled results. Above 175 km for orbit 1386 and 200 km for orbit 1485 there is a deviation between the model and the data.

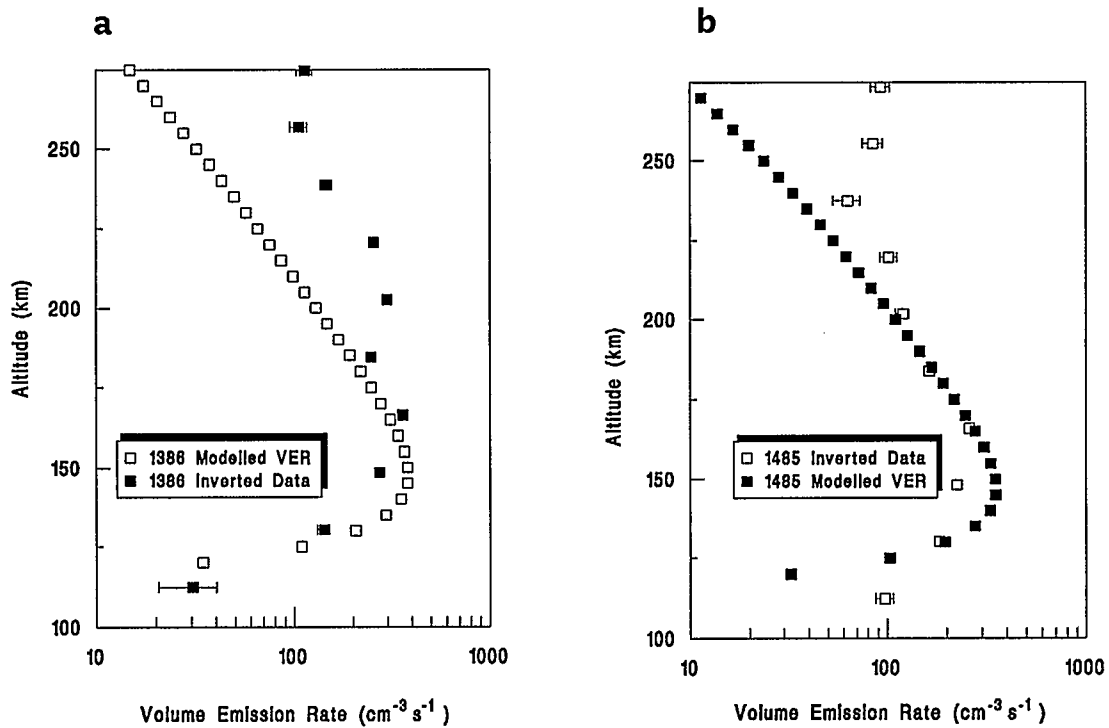


Figure 5.10 A comparison of altitude/VER profiles obtained from the Viking satellite and the model for orbits a) 1386 99.019 b) 1485 99.032

5.3.2 Comparison of Column Intensity Profiles

The data from the Viking satellite was compared to data obtained from the model. While direct comparison between models and calculations is possible in monochromatic sources, Viking observed a range of wavelength. Thus, direct comparison of the two data sets would not be correct since the camera has a wavelength sensitivity. Thus, during the calculation, the model also calculated the data numbers (DN) that the camera would observe from an emission.

Figure 5.11 shows the measured sensitivity curve (Vallance Jones, 1986) for camera 0. The original curve of Vallance Jones gave the sensitivity in DN/photon. This value was multiplied by 653, the number of photons that one kilorayleigh would produce, a value that Vallance Jones determined (Vallance Jones, 1986). The curve also has a wavelength sensitivity. Thus during the model calculation it was necessary to calculate all of the LBH emission bands separately and multiply the emission at that wavelength by the camera sensitivity, in DN/kR. Then all of the DN at a given altitude were summed to give the observed DN at an altitude. Figure 5.12 shows the calculated altitude/DN curves for both Viking orbits.

Figure 5.13 shows the altitude corrected/intensity profile for the observed Viking data. In this case, the higher altitude peak was shifted down to an altitude of 135 km. When this is done, the altitude of the lower peak is at 9 km in both cases, indicating that this emission may be due to tropospheric processes.

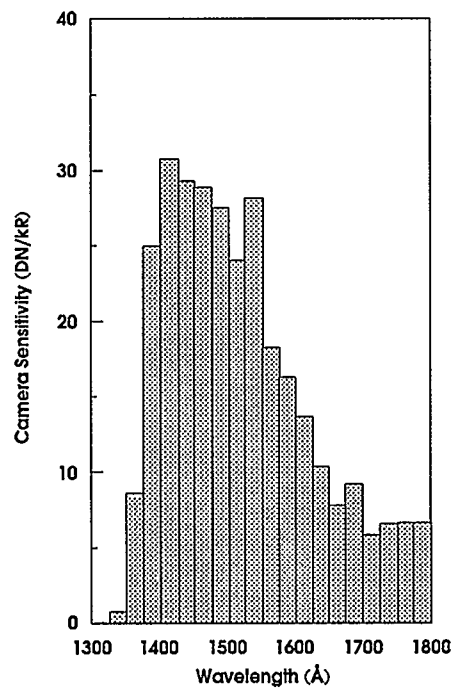


Figure 5.11 Camera 0 sensitivity as a function of wavelength

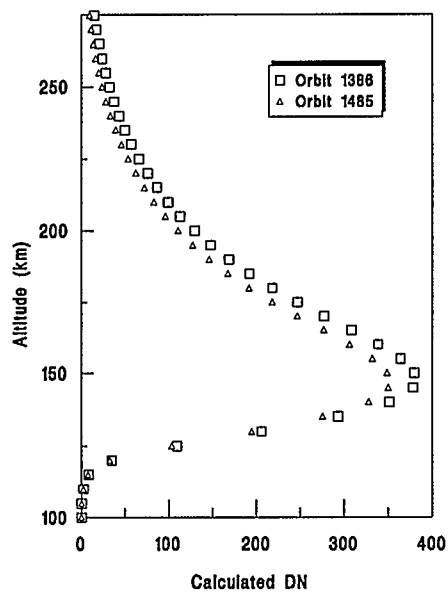


Figure 5.12 Modelled altitude/DN profiles for orbits 1386 and 1485

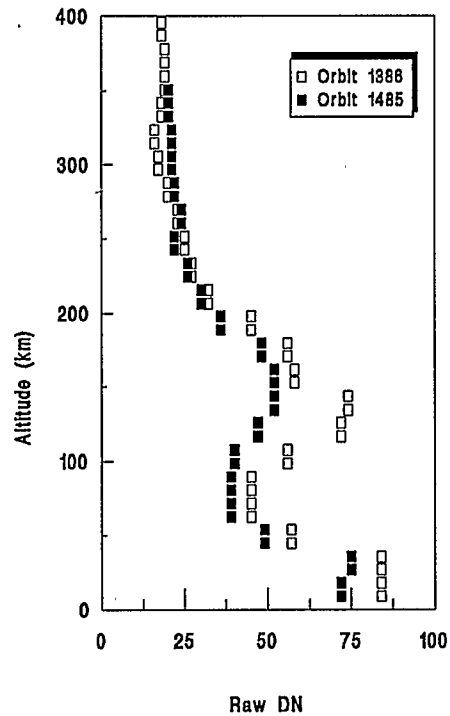


Figure 5.13 Altitude corrected/intensity profiles for Orbits 1386 and 1485

Figure 5.14 shows a comparison between the altitude and the ratio of the calculated DN to the observed DN. The observed DN have been altitude corrected so that the higher altitude peak occurs at an altitude of 135 km. If there is a constant correction factor, then the curve would be a vertical line. In this case, the plot is not vertical, but changes with altitude. This indicates that there is not a simple relationship between the calculated and observed profiles.

Figure 5.15 shows the altitude/calculated DN profile for orbits 1386 and 1485. This plot uses normalized DN due to the large difference between the observed and the calculated DN. The uncorrected and altitude corrected observational data are plotted along with the

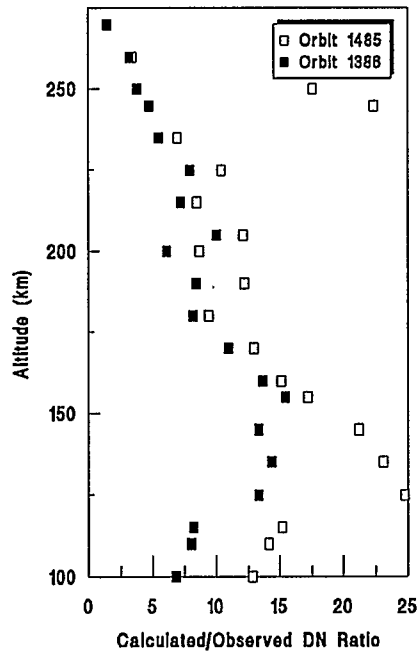


Figure 5.14 Altitude/DN Ratio for orbits 1386 and 1485

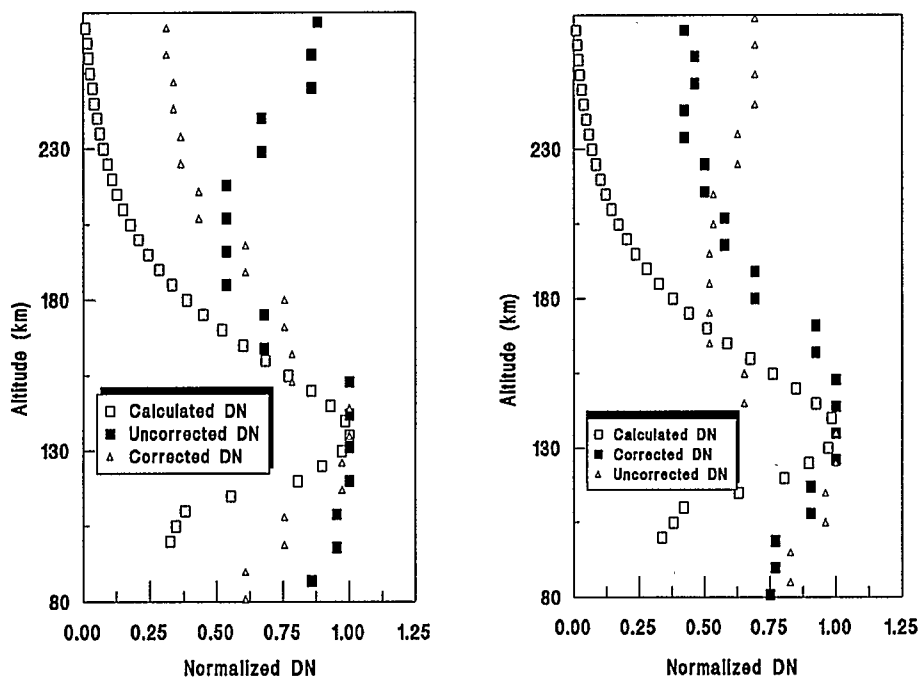


Figure 5.15 A comparison of altitude/normalized DN for the calculated profile, Altitude corrected and uncorrected observed profiles for
a) Orbit 1386 b) Orbit 1485

calculated values. The uncorrected data does not have the same shape as the altitude corrected data at lower altitudes or at higher altitudes. The altitude corrected data have the same shape as the calculated profile at lower and higher altitudes, although they are shifted to higher values. This would indicate that the calculated and corrected profiles may have the same origin. The differences in the shapes may be caused by leakage of emissions from other wavelengths, resulting in a general displacement of the observed curve. Griffioen et al. (1991) have found that there is leakage of light in the 190 nm to 340 nm range.

Chapter 6 Conclusions and Future Work

6.1 Conclusions

The purpose of this study was to develop a simple model which explains the observed altitude/intensity profiles that have been observed by the Viking satellite. The basis for any model of dayglow is the photoelectron flux calculation. This model is based upon the simple photoelectron flux model of Richards and Torr (1983). It was chosen because it computes very quickly, due to simplifying assumptions made about the secondary photoelectron production. It is based on photoelectron measurements made in 1975 and 1976, as are the other photoelectron flux models (Meier, 1991). It has been found that there can be as much as a factor of two difference between the measured and calculated fluxes (Meier, 1991), indicating that this model is probably as correct as the other models.

Also required for the simple model are neutral densities and neutral temperatures, which are calculated using the MSIS-86 model (Hedin, 1987). Electron densities are calculated using the model of Rasmussen et al. (1988). The cross sections for the LBH calculations were those of Ajello and Shemansky (1985). For OI 1356, the cross sections of Stone and Zipf (1974) are used. Finally, the EUV flux is determined using the model of Tobiska and Barth (1990).

From all of these different models a simple model to calculate the EUV dayglow was constructed. It calculates the volume emission rates for the different species as well as column intensities and slant column intensities, i.e. the intensities that rockets and satellites would view. To verify that the model was valid, it was compared to published observational data of Link et al. (1988). The model and the other work compared favourably, down to an altitude of 140 km for OI 1356 and 160 km for the 144.5 nm LBH band. Unfortunately, all of the LBH data that appears in the literature is based upon monochromatic line sources. Below these altitudes, the calculated column intensities were high, due to inaccuracies in the O₂ absorption.

The results from the model also match the results that Meier (1991) published. The results from the model and Meier (1991) have the same curve shapes, similar intensity and volume emission rate values. This is true for the altitude/volume emission rate, the altitude/intensity and the tangent altitude/slant column emission rates curves.

The data that was obtained from the Viking satellite did not match any of the calculated profiles or any of the profiles that appear in the literature. It was initially found that the altitude/intensity plots have two peaks, one at approximately 120 km and the second above 200 km. When the altitudes were adjusted so that the second peak's altitude was the same as the model's, the first peak occurred at 10 km. This would indicate that the troposphere could be the source of the emissions.

Using these corrected altitude/intensity profiles, agreement was found between the calculated and the inverted volume emission rate when the auroral conversion factor of 14 ± 2 DN/kR of Jones et al. (1987) was applied to the data. The inverted profiles had emissions below 120 km, which cannot be explained by the model.

The calculated tangent altitude/slant intensities profiles were significantly larger than the corrected Viking profiles, as were the calculated altitude/DN intensity profiles, which were calculated using the measured camera sensitivity. Since the differences could not be resolved, a comparison was made between the normalized profiles. It was found that the Viking profiles have a similar shape to the calculated. The differences between the two profiles were thought to be due to longer wavelength leakage of the camera.

The initial purpose of the study was to develop a simple model for EUV dayglow, which has been accomplished. The results from the simple model compare favourably to those obtained from more complicated models. Appendix 2 shows an outline of the computer model. This model has a very fast computational time, typical runs required approximately 15 seconds of user time on a MIPS RS2030 workstation. This model supports diagnostic work on limb images obtained from satellites or from data collected from rockets. It can easily be expanded to include more species in the profile calculations or narrowed to calculate profiles from a monochromatic source.

6.2 Future Work

While a functional diagnostic model has been obtained, improvements can be made to it. A better calculation of Shumann-Runge absorption could be included in the model. A better photoelectron flux model could also be included, one that includes a detailed calculation of secondary photoelectron flux. While these two improvements might improve the accuracy of the model, they would remove the rapid computational speed that the present model possesses.

Using the present model, it would be possible to calculate the EUV dayglow emissions that a top down satellite would observe over a large geographic area. This would allow for dayglow contamination to be subtracted from the existing Viking images. This could allow for other more detailed work to be performed on the auroral images, possibly revealing yet undiscovered auroral phenomena.

References

- Ajello, J.M. and D.E. Shemansky, A Reexamination of Important N₂ Cross Sections by Electron Impact With Application to the Dayglow: The Lyman-Birge-Hopfield Band System and NI (119.9 nm), J. Geophys. Res., 90, 9845, 1985.
- Anger, C.D., S.K. Babey, A.L. Broadfoot, R.G. Brown, L.L. Cogger, R.L. Gattinger, J.W. Haslet, R.A. King, D.J. McEwen, J.S. Murphree, E.H. Richardson, B.R. Sandel, K. Smith and A. Vallance Jones, An Ultraviolet Auroral Imager for the Viking Spacecraft, Geophys. Res. Let., 14, 387, 1987.
- Banks, P.M. and G. Kockarts, *Aeronomy Part A*, Academic Press, New York, 1973.
- Chamberlain, J.W. and D.M. Hunten, *Theory of Planetary Atmospheres, An Introduction to Their Physics and Chemistry*, vol. 36, *International Geophysics Series*, Academic Press, Toronto, 1987.
- Conway R.R., Self Absorption of the N₂ Lyman-Birge-Hopfield Bands in the Far Ultraviolet Dayglow, J. Geophys. Res., 87, 859, 1982.
- Conway, R.R. and A.B. Christensen, The Ultraviolet Dayglow at Solar Maximum 2. Photometer Observations of N₂ Second Positive (0,0) Band Emission, J. Geophys. Res., 90, 6601, 1985.

Conway R.R., D.K. Prinz and R.E. Huffman, Abundance of Atomic Oxygen in the Lower Thermosphere from Satellite Observations of the OI 1641 Å Dayglow, Planet. Space Sci., 36, 963, 1988.

Duhau, S. and M. C. Azpiazu, Empirical Model of the E-Region Electron Temperature around noon and at Low Magnetic Activity, Planet. Space Sci., 33, 909, 1985.

Gerald, C.F. and P.O. Wheatley, *Applied Numerical Analysis*, Addison-Wesley, New York, 1990.

Griffioen, E., J. McConnell, J. Murphree, G. Sheperd, L. Cogger and A. Vallance Jones, Viking UV cameras: Calibration using model calculations and long wavelength leakage , Can. J. Phys., 69, 1154, 1991.

Hedin,A.E., A Revised Thermospheric Model Based on Mass Spectrometer and Incoherent Scatter Data: MSIS-83, J. Geophys. Res., 88, 170, 1983.

Hedin, A.E., MSIS-86 Thermospheric Model, J. Geophys. Res., 92,4649, 1987.

Hernandez, S.P., J.P Doering, V.J. Abreu and G.A. Victor, Comparison of Absolute Photoelectron Fluxes Measured on AE-C and AE-E with Theoretical Fluxes and Predicted and Measured N₂ 2PG

3371 Å Volume Emission Rates, Planet. Space Sci., 31, 221, 1983.

Hinteregger, H.E., K. Fukui and B.R. Gilson, Observational, Reference and Model Data on Solar EUV from Measurements on AE-E, Geophys. Res. Letters, 8, 1147, 1981.

Hultqvist, B., The Viking Project, Geophys. Res. Letters, 14, 379, 1987

Jacchia, L.G., Revised Static Models of the Thermosphere and Exosphere with Empirical Temperature Profiles, Smithsonian Astrophys. Obs. Spec. Rept., 322, 1971.

Jacchia, L.G., Thermospheric Temperature, Density and Composition: New Models, Smithsonian Astrophys. Obs. Spec. Rept., 375, 1977.

Jones, A.V., R.L. Gattinger, F. Creutzberg, R.A. King, P. Prikryl, L.L. Cogger, D.J. McEwen, F.R. Harris, C.D. Anger, J.S. Murphree, and R.A. Koehler, A Comparison of Canopus Ground Optical Data with Images from the Viking UV Camera, Geophys. Res. Lett., 14, 391, 1987.

Kopp, J.P., P.W. Rusch, R.G. Roble, G.A. Victor and P.B. Hays, Photoemission in the Second Positive System of Molecular Nitrogen in the Earth's Dayglow, J. Geophys. Res., 82, 555, 1977.

Link, R., G.R. Gladstone and S. Chakrabarti, A Reanalysis of Rocket Measurements of the Ultraviolet Dayglow, J. Geophys. Res., 93, 14631, 1988

Meier, R.R., Ultraviolet Remote Sensing of the Upper Atmosphere, Space Sci. Rev., 58,1, 1991.

Meier, R.R. and D.E. Anderson, Determination of Atmospheric Composition and Temperature from the UV Dayglow, Planetary Space Sci., 31, 967, 1983

Meier, R.R., D.J. Strickland, P.D. Feldman and E.P. Gentieu, The Ultraviolet Dayglow 1. Far UV Emissions of N and N₂, J. Geophys. Res., 85, 2177, 1980.

Meier, R.R., Conway, R.R., D.E. Anderson, P.D. Feldman, R.W. Eastes, E.P. Gentieu and A.B. Christensen, The Ultraviolet Dayglow at Solar Maximum 3. Photoelectron-Excited Emissions of N₂ and O, J. Geophys. Res., 90, 6608, 1985.

Meyerott, R.E. and G.R. Swenson, A Surface Chemistry Model for the Production of N₂ LBH Spacecraft Glow, Planetary Space Sci., 38, 555, 1990.

Morrison , M.D., C.W. Bowers, P.D. Feldman and R.R. Meier, The EUV Dayglow at High Spectral Resolution, J. Geophys. Res., 95, 4113, 1990.

Oran, E.S. and D.J. Strickland, Photoelectron Flux in the Earth's Ionosphere, Planetary Space Sci., 26, 1161, 1978.

Rasmussen, C.E., R.W. Schunk and V.B. Wickwar, A Photochemical Equilibrium Model for Ionospheric Conductivity, J. Geophys. Res., 93, 9831, 1986.

Rees, M.H., *Physics and Chemistry of the Upper Atmosphere*, Cambridge University Press, New York, 1989.

Richards, P.G. and D.G. Torr, A Simple Model for Calculation and Parameterizing the Ionospheric Photoelectron Flux, J. Geophys. Res., 88, 2155, 1983.

Rochon, Y, The WINDII Project: An Atmospheric Inversion Model for Winds and Temperatures, unpublished CREES report, 1985.

Rottman, G.J., Observations of Solar UV and EUV Variability, Adv. Space Res., 8, 53, 1988.

Schunk, R.W. and W.J. Raitt, Atomic Nitrogen and Oxygen Ions in the Daytime High-Latitude F Region, J. Geophys. Res., 85, 1255, 1980.

- Stone, E.J. and E.C. Zipf, Excitation of Atomic Nitrogen by Electron Impact, J. Chem. Phys., 58, 4278, 1973.
- Stone, E.J. and E.C. Zipf, Electron Impact Excitation of the $^3S^o$ and $^5S^o$ States of Atomic Oxygen, J. Chem. Phys., 60, 4237, 1974.
- Strickland, D.J. and R.R. Meier, A Photoelectron Model for Rapid Computation of Atmospheric Excitation Rates, N.R.L. Memorandum Report 5004, 1982.
- Strickland, D.J., J.R. Jasperse and J.A. Whalen, Dependence of Auroral FUV Emissions on the Incident Electron Spectrum and Neutral Atmosphere, J. Geophys. Res., 88, 8051, 1983.
- Tobiska, W.K. and C.A. Barth, A Solar EUV Flux Model, J. Geophys. Res., 95, 8243, 1990.
- Torr, M.R., D.G. Torr, R.A. Ong and R.E. Hinteregger, Geophys. Res. Letters, 6, 771, 1979.
- Vallance Jones, A., Viking Camera Calibration, unpublished report, 1986.
- Vidal-Madjar, A., Evolution of the Solar Lyman Alpha Flux During Four Consecutive Years, Solar Phys., 40, 69, 1975.

Vidal-Madjar, A. and B. Phissamay, The Solar Lyman Alpha Flux Near Solar Minimum, Solar Phys., 66, 259, 1980.

Appendix 1 Viking Orbits Which Contain Double Limbs

Orbit	Frame No.	Auroral Contamination	Location of Auroral Contamination	Star	Location of Star	Comments
1358	99.021	yes	R. center	yes?	on upper l	clear d.l on L.
1358	99.022	yes	center and R.	no		clear dl on L.
1364	99.005	yes	heavy? in center	no		clear dl on R.
1364	99.006	yes	moving to center	yes	center near top	
1364	99.007	yes	both limbs	yes	center near top	
1380	99.017	yes	both limbs in center			
1380	99.018	yes	center on both limbs	yes	upper center	clear dl on L
1380	99.019	yes	center on both limbs	yes	L center above dl clear dl on L	
1380	99.020	yes	center on both limbs	yes	in limb, ac present clear dl on L	
1385	99.032	yes	L and center of dl	no		clear dl on R

Orbit	Frame No.	Auroral Contamination	Location of Auroral Contamination	Star	Location of Star	Comments
1385	99.033	yes?	center and L, heavy?	no		heavy ac? or image problems?
1385	99.034	yes?	center?	yes	L top of image	clear dl on R heavy ac? or image problems
1385	99.035	yes	center and R	yes	L top of image down dl on far L	
1386	99.019	yes	center and L	no		dl on R clear
1386	99.020	yes	center and L	no		clear dl on R, hazy
1386	99.021	yes	lower limb center & L	no		clear dl on R, hazy
1386	99.022	yes	lower center & L	no		hazy dl not as wide as prvs, dl
1386	99.023	yes?	lower L	yes	top L	one to work with
1386	99.024	no		yes	L just above upper limb one to work	
1386	99.025	???	bottom of screen	yes?	in 'limb'	single limb?

Orbit	Frame No.	Auroral Contamination	Location of Auroral Contamination	Star	Location of Star	Comments
1386	99.026	???	???	???		what is this?
1386	99.027	???				
1391	99.027	yes	lower center and L	no		clear on R
1391	99.028	yes	L both limbs			clear on far R
1391	99.029	yes	entire dl	no		
1396	99.018	yes	both limbs	no		clear on R
1396	99.019	yes	both limbs	no		very hazy, imaging problems?
1396	99.020	yes	both limbs center & R	yes	L near top	clear on L
1396	99.021	yes	both limb on R	yes	L top	clear L dl
1396	99.022	yes	R side	yes	L in upper limb clear L dl, star occultation	

Orbit	Frame No.	Auroral Contamination	Location of Auroral Contamination	Star	Location of Star	Comments
1397	99.008	yes	lower center and L	yes	center top of image no clear dl at all	
1397	99.009	yes	entire dl	yes	two stars center & L complete A.C.	
1397	99.010	yes	entire dl	yes	two stars hidden in AC no clear dl	
1402	99.028	yes	entire dl	yes	L 1/2 way bet dl & top no dl visible at all	
1402	99.029	yes	entire dl	yes	L 2/3 way bet dl & top no dl visible at all	
1413	99.017	no		no		hazy? use this one?
1413	99.018	yes	entire dl?	yes	upper L of image hazy use this one??	
1413	99.019	yes	entire dl?	yes	in dl	hazy? star occultation
1430	99.027	no		no		v. clear dl.
1430	99.028	yes	entire dl!	no		hazy?

Orbit	Frame No.	Auroral Contamination	Location of Auroral Contamination	Star	Location of Star	Comments
1430	99.029	yes	entire dl	yes	upper L	hazy?
1430	99.030	yes	entire dl?	yes	just above dl on L hazy?	
1485	99.032	no?		no		very clear dl? if clear of AC use it
1485	99.033	no		no		AC below lower dl use it!!
1485	99.034	yes	lower L dl	no		hazy, R dl clear
1485	99.035	yes?	L side	no		hazy
1485	99.036	yes	entire dl	no		hazy
1485	99.037	yes?	entire dl	yes	2 stars, 1 bright, 1 R clear on far L	
1485	99.038	no?		yes	2 stars 1 bright single limb or v. faint	
1490	99.031	no?		no		v. hazy

Orbit	Frame No.	Auroral Contamination	Location of Auroral Contamination	Star	Location of Star	Comments
1490	99.032	yes?	R side	yes	upper R side	clear dl on L
1490	99.033	no?		yes	1 br 1 faint on R ab dl clear of AC use!!!	
1501	99.026	yes	lower L side	no		R side clear
1501	99.027	yes	entire lower l	no		
1501	99.028	yes	entire limb	no		
1501	99.029	yes	center and R of limb	yes	upper R side	L side clear
1501	99.030	yes	center and R of limb	yes	2 1 br 1 faint R side L side clear	
1512	99.029	yes?	center and R	no		slanted limb
1512	99.030	yes	center and R	no		slanted limb
1512	99.031	no?		yes	bright one top	hazy

Orbit	Frame No.	Auroral Contamination	Location of Auroral Contamination	Star	Location of Star	Comments
1512	99.032	no?		yes	bright one	hazy
1529	99.022	yes?	lower limb	no		hazy, slanted
1529	99.023	yes?	moving to upper limb	no		slanted
1529	99.024	yes	entire limb	no		slanted, hazy, baffel covering 1/2 image
1529	99.025	yes	entire limb	no		hazy, slanted, baffel covering 1/2 image
1534	99.022	yes	lower l and some upper yes?	center upper l	hazy, slanted, clear on R	
1534	99.024	yes	entire limb	yes?	center upper limb hazy, slanted	
1534	99.026	yes	upper limb	no		hazy, slanted, baffel covering 1/2 dl
1540	99.026	yes?	lower limb	yes?	center above dl (X2) slanted, hazy	
1540	99.027	yes?	lower limb	yes?	center just above dl (X2) hazy below	

Orbit	Frame No.	Auroral Contamination	Location of Auroral Contamination	Star	Location of Star	Comments
1540	99.028	yes?	lower limb	yes?	in dl	hazy below dl, slanted, clear R side
1540	99.029	yes?	lower limb	yes?	in dl	hazy below dl, slanted
1540	99.030	yes?	entire limb	yes?	in dl	hazy, slanted
1551	99.033	yes	entire dl	no		
1573	99.026	yes?	lower dl	yes	2-1 L,2- center upper l hazy below lower l,	
1573	99.027	yes?	lower dl	yes	L upper l,2-center in ll hazy,slanted	
1573	99.028	yes?	entire dl	no?		slanted
1573	99.029	yes?	entire dl	no?		slanted
1573	99.030	yes	entire dl	no?		slanted
1578	99.020	yes?	lower dl	yes	L side above dl slanted	

Orbit	Frame No.	Auroral Contamination	Location of Auroral Contamination	Star	Location of Star	Comments
1578	99.021	yes?	entire dl	no?		slanted
1578	99.022	yes	entire dl	no?		slanted, hazy
1578	99.023	no		no		slanted. baffel blockage R side of dl
1584	99.012	no		yes	2-1 L 2 center	slanted clear R, use
1584	99.013	yes	lower L l	yes	2-1 L 2 center in dl? slanted, use!!!	
1584	99.014	yes	entire lower l	no?		slanted
1584	99.015	yes	entire dl	no		slanted
1584	99.016	yes	entire dl	no		slanted, baffel cuts 1/3 dl
1589	99.010	no?		no		slanted, hazy
1589	99.011	no?		no		slanted, hazy, baffel cuts off 1/2 dl

Orbit	Frame No.	Auroral Contamination	Location of Auroral Contamination	Star	Location of Star	Comments
1595	99.026	yes	lower l	no		slanted, R clear
1595	99.027	yes	lower l	no		slanted
1595	99.028	yes	entire dl	no		slanted, hazy
1600	99.010	yes	entire dl	no		slanted
1600	99.011	yes	entire dl	no		slanted
1601	99.014	no		yes	2-1 center 2 R ab ul slanted, aurora below	
1601	99.015	no		yes	1 center just ab dl slanted, aurora just	
1601	99.016	no		yes	1 center in upper l slanted, aurora	
1606	99.016	yes	entire dl	no		slanted
1611	99.024	yes	upper l	no		slanted, baffel contamination on upper 1/3

Orbit	Frame No.	Auroral Contamination	Location of Auroral Contamination	Star	Location of Star	Comments
1758	99	yes?	lower l	yes	R side, 3 in center? clear dl on R	
1758	99.001	yes?	lower l	yes	upper R	clear dl on R

Appendix 2 Computer Model Outline

